PONTIFICIA UNIVERSIDAD CATÓLICA DE CHILE
FACULTAD DE FÍSICA
INSTITUTO DE ASTROFÍSICA

Exploring the intersection of Lyman-α Emitters & Lyman Break Galaxies behind the strongly lensed clusters: Abell370, Abell2744 and MACS0416.

BY

GONZALO PRIETO LYON

Tesis presentada a la Facultad de Física de la Pontificia Universidad Católica de Chile, para optar al grado académico de Magíster en Astrofísica.

SUPERVISORS	:	Dr. Franz Bauer & Dr. Lucia Guaita
CORRECTORS	:	Dr. Felipe Barrientos
CORRECTORS	:	Dr. Valentino Gonzalez

August 6th, 2021

Santiago, Chile

Declaration

Acknowledgements

Thanks to my family for their care and support, specially during these harsh years.

I would like to express my deepest thanks to both of my supervisors, Professor Franz Bauer and Dr. Lucia Guaita for having me as their student all these years, teaching me with patience and care, and preparing me for my future. My thank you to Professor Leopoldo Infante for introducing me to the topic of extragalactic astrophysics and always being there for me. And thank you to all the students, staff, and professors at the institute of astronomy at PUC for making it such a welcoming environment.

I also would like to acknowledge the Millennium Science Initiative (MAS) for funding my Master's Degree and this project.

Contents

List of Tables

List of Figures

Abstract

In this thesis, we present a study of star-forming galaxies between redshifts 2.9-6.7 split among four categories: Pure LAEs (73 galaxies) without UV detection; Pure LBGs (1015 galaxies) without Lyman-α detection; LAE-LBGs (193 galaxies), with both Lyman break and Lyman-α detected; and *Other SFGs* without any of these signatures (459 galaxies). We use Multi-Unit Spectroscopic Explorer (MUSE) and legacy Hubble Space Telescope (HST) data of the three Hubble Frontier Fields lensing clusters A370, A2744 and MACS0416, reaching magnitudes as faint as $M_{1500} \approx -13$. We study the continuum and emission-line parameters of our sample, with the goal of finding and understanding any intrinsic differences between the aforementioned regimes of SFGs. We report a great diversity of high-redshift galaxies in the Lyman-α - M_{1500} plane, with a lack of massive galaxies above the SFR(Lyα)=SFR(UV) line at $M_{1500} < -18$, with most pure LAEs near this line and $\log(L_{Ly\alpha})$<42.0. We measure the UV slope of pure LBGs and LAE-LBGs, with median values of β=-1.75 and β=-2.44 respectively, meaning that LAEs overall are near the dust-free domain while pure LBGs tend to be redder, and hence presumably more dust-obscured and/or older, the former being one of the probable reasons for their lack of Lyman-α; SFGs without LB or Lyα show redder median slopes of β=-1.59. LAE-LBGs tend to have a stronger sSFR than pure LBGs and other SFGs by a factor of 2 at every studied redshift. We find slight differences between the two LAE populations, with LAE-LBGs showing broader Lyman-α profiles, but further radiative transfer simulations are needed to clarify the contribution of HI velocity and column density.

Chapter 1

Introduction

1.1 Importance of Lyman-α Emitters

We define a Lyman Alpha Emitter (LAE) as a galaxy which has a Lyman-α line in emission. These galaxies are a great tool for the study of the Universe, especially at high redshift. In fact, high-redshift galaxies can be very faint in the rest-frame UV continuum but very bright in Lyman-α. Therefore through Lyman-α, we can probe some of the faintest galaxies in the Universe, trace some of their key physical properties, and even study the structure of the IGM.

Faint galaxies at z$\gtrsim$7 are of special interest for the study of the epoch of reionization (EoR) (e.g. Ishigaki et al. (2018)), since massive and intrinsically bright galaxies do not produce enough ionizing radiation to explain the reionization of the IGM without the contribution of less massive and fainter galaxies (e.g. Bouwens et al. (2015), McLure et al. (2013)). In many cases, it is not possible to detect the UV continuum emissions of faint galaxies of $M_{1500,UV}$>-17 without extensive observation times. A way to study the galaxies that populate the faint-end of the luminosity function is through LAEs (de La Vieuville et al. (2019)). Due to its sometimes high equivalent width, the Lyman-α emission lines can be visible even when the UV continuum is not, letting us probe further into the domain of UV faint galaxies. If we further add a strong gravitational lensing to this, produced by massive galaxy clusters such as Abell 380, Abell 2744 and MACS0416, we are able to reach to even fainter magnitudes $M_{1500,UV}$=-13 (e.g. this work and Livermore et al. (2017)). It is also possible to measure the structure and morphology of the IGM near the EoR and of reionization

bubbles through LAEs (e.g. Hu et al. (2021),Mason & Gronke (2020)).

The Lyman-α emission by itself carries a lot of information about the physical properties of the galaxy, starting from information of the ionizing young stellar population that excites the neutral hydrogen (HI) to the kinematics and distribution of the HI gas from where it is re-emitted. Such properties and more, which we will discuss further next, are contained in the Lyman-α line profile (Verhamme et al. (2006)).

1.2 Uniqueness of the Lyman-α profile

The emission and transmission of Lyman-α is a complex problem involving multiple variables, from the dust content of the ISM, to the same HI gas from where it is emitted. Lyman-α has a similar origin to the UV continuum of galaxies, the ionizing radiation of young stars. This radiation will excite the HI gas surrounding the star-forming regions, which later will spontaneously fall from the n=2 orbital to the ground state, producing a Lyman-α photon. Since Lyman-α can be absorbed from the same HI gas where it is formed, an interesting effect takes place, called resonant scattering.

We talk about resonant scattering when a photon has a higher cross section near the potential of a given transition, making it easier to be absorbed than other photons with more dissimilar energies. This makes the scattering optical depth higher, trapping photons in a random walk with a short free path until they gain or lose energy via doppler-effect and reach a lower scattering cross section, effectively escaping. For the case of Lyman-α a photon that is captured by an Hydrogen atom in movement, will then be stochastically re-emitted in a different direction. The relativistic Doppler effect due to the velocity of the atom at the time of emission will then result in a change of wavelength from the perspective of the observer. Given enough scattering events, an emission line will broaden due to this effect. There are two main factors that decide the strength of the broadening due to resonant scatter: HI velocity and HI column density.

There are a variety of factors that contribute to the velocity of the HI gas. The most fundamental

factor when studying Lyman-α will be the outflow of neutral gas due to the ongoing star formation, which we can theoretically understand as an expanding HI shell (e.g. Gronke et al. (2015)). There are also other sources of velocity that can affect the HI gas, such as rotation (e.g. Garavito-Camargo et al. (2014)), and inflowing streams of material (e.g. Wisotzki et al. (2018)). All of these velocity components can increase the broadening of Lyman-α due to a higher velocity of the atoms that will re-emit it.

The number of resonant scattering events will be dictated by the amount of neutral hydrogen in the path of the photons, meaning that the column density of HI is of great importance to the shape of Lyman-α (Gurung-López et al. (2019)). A higher column density of neutral gas ($N_{\rm HI}$) will make it extremely hard for Lyman-α to propagate at its rest-frame wavelength, commonly resulting in a complete absorption of emissions at rest-frame 1216Å with some wavelength spread. This can result in Lyman-α taking a double-peaked shape, with a "red" peak at $\lambda > 1216$Å and a "blue" peak at $\lambda < 1216$Å. In cases where the column density is low, it is possible for Lyman-α to escape at its systemic redshift. On the other hand, a high value of $N_{\rm HI}$ will obscure the profile, sometimes even capturing the emission from the blue peak completely.

One of the reasons why Lyman-α is such an important feature is that the kinematic and column density information of the neutral hydrogen will be imprinted into its profile, giving it a characteristic shape depending on their contributions. However, it is not straightforward to disentangle the effects of HI velocity and column density, since both are at play when shaping the Lyman-α profile, as well as extinction by interstellar dust. Only by more complex radiative transfer simulations of Lyman-α is it possible to understand how these two factors individually give shape to the profile. Nonetheless, there are many conclusions we can draw by directly studying the emission line profile shape, as we will see in this work.

Aside from the effects of the ISM on Lyman-α, there is also an important role of the IGM on its shape. In cases where there is a high amount of neutral hydrogen between the galaxy in question and the observer, there will be a strong absorption due to the neutral hydrogen, commonly generating a loss of all the emission below rest-frame 912Å in the form of a Lyman Forest or a

Gunn–Peterson trough (Dijkstra (2014)). The blue peak of the Lyman-α profile will be more easily observable at lower redshifts, and as we approach higher redshifts near the EoR, the percentage of neutral hydrogen gets higher, making it extremely rare for a $z \sim 7$ to have a detectable blue peak, except for cases of strong ionization bubbles due to a single bright source and/or multiple fainter sources which ionize the surrounding hydrogen (e.g. Matthee et al. (2018) and Meyer et al. (2020)).

1.3 Diversity of high redshift galaxies

When observing the Universe, we can find that the intrinsic properties of galaxies can vary wildly from one to another; these changing parameters can include physical properties such as stellar mass, luminosity, gas reservoirs, and dust ratios as well as different morphologies, among others. This results in a great diversity of galaxies in the Universe, from low-mass dwarf galaxies to massive elliptical galaxies, we may find galaxies that have a powerful radio emission or galaxies that have an active supermassive central black hole. The redshift or epoch where galaxies are situated in time is also strongly related to the types of galaxies that we may find; for example, we are much more likely to find a quiescent galaxy in a more local environment than near the epoch of reionization, where we most likely will find galaxies that have not depleted their gas reservoirs and still have a relatively high formation rate of stars. In this work we will focus our interest on the last type of galaxy mentioned, star-forming galaxies.

We can label galaxies as star-forming galaxies or SFGs, if they are situated in the main sequence, which is the tight relation between star formation rate and stellar mass of galaxies. We define star formation rate (SFR) as the total stellar mass formed per year in a galaxy, normally measured in solar masses per year ($M_{\odot}/yr$). The change of SFR in a galaxy over its life is then called star formation history (SFH). For a galaxy to be in the main sequence it needs to have a steady star formation rate which is proportional to its stellar mass (this ratio of SFR/M_* is knows as specific star formation rate, or sSFR), forming a tight direct relation between both properties in the form of a power law $log(SFR) = A(z)log(M_*) + B(z)$, where the slope and normalization parameter depend on the age of the Universe (Speagle et al. (2014)).

We expect SFGs to have vast reservoirs of hydrogen gas in the ISM to provide the material for a steady formation of stars. We can also label galaxies with low sSFR, that are below the main sequence, as quiescent or dead galaxies and those that have high sSFR as starburst galaxies. This definition of SFGs is valid for even at early epochs of the Universe as shown by Santini et al. (2017), who show that the MS relation holds up to $z \sim 6$.

Two of the main methods for the detection of high redshift SFGs are by observing their Lyman Break and/or their Lyman-α emission. The Lyman Break consists in the strong absorption of UV emission below the Lyman limit (912Å) due to the neutral hydrogen present in the IGM (Madau (1995)), as the light travels and it goes through HI clouds at different redshifts (distances) the observed wavelength of the galaxy by these clouds will be redshifted, causing the hydrogen absorption lines to continuously absorb light in different wavelengths below rest-frame Lyman-α, this feature is called Lyman-Alpha Forest. This absorption is useful to study the HI gas line of sight (LoS) distribution of the IGM by observing QSOs (Rauch (1998)), but most importantly for the purpose of this work is the flux difference, or break, that the absorption leaves after and before Lyman-α. We call this the Lyman Break, and its observed wavelength is a key indicator of the redshift of a galaxy, whereby we can calculate a photometric redshift by comparing the difference between the magnitude of filters before and after the break (Fontana et al. (2000)), the accuracy of the photometric redshift will depend on how narrow the filters are. Due to its simple break shape, it is possible to confuse it with the Balmer break (3645Å) and/or the 4000-Å break (due to Ca H+K), causing low redshift faint galaxies to be confused for high redshift galaxies. Follow-up spectroscopy of galaxies photometrically selected by their Lyman break can help refine the redshift (i.e. bye emission lines such as Lyman-α, CIII, MgII), contamination fraction, and properties (SFR, M_*, metallicity, among others). A second method to detect high redshift galaxies is to measure their Lyman-α more directly, and calculate z_{spec} more accurately. This method is possible since Lyman-α can be an incredibly bright feature, in some cases reaching $L_{Ly\alpha}$=10^{43} erg s^{-1}, making it detectable even from some of the most distant galaxies. Moreover, its unique line profile makes it easier to identify. Nonetheless, due to the radiative transfer of Lyman-α, its peak might be shifted from the systemic redshift of the galaxy, making it sometimes inaccurate by a very small margin (e.g. Shapley et al. (2003), Verhamme et al. (2018)).

From these two features we define three particular regimes of SFGs, pure Lyman Break Galaxies (pure LBGs), pure Lyman Alpha Emitters (pure LAEs), galaxies that have both of these features (LAE-LBGs), all of these are prevalent at high redshifts. We also define a fourth regime of galaxies that do not show a Lyman-α emission or a Lyman Break, we call these "*Other SFGs*". One of the main topics we are interested in discussing is the diversity of high redshift SFGs. We seek to gain deeper insight into the reasons why some galaxies may present a detectable Lyman-α emission and others do not. For this purpose, we study both the Lyman-α emission of these galaxies, their UV continuum, and the derived physical properties, such as SFR and stellar mass. Learning about the different properties of these galaxies and their interstellar environments can also teach us about galaxy evolution and diversification during the earlier epochs of the Universe.

1.4 A great tool: Strong Lensing

For this work we aim to study three fields, Abell 2744, Abel 370 and MACSJ0416. One of the properties that make these fields especially interesting is that the presence of massive low-redshift clusters (z = 0.3 $\sim$ 0.4) can facilitate the study of high-redshift galaxies due to the strong lensing effect and the large area they cover. For this reason, they have been extensively studied in previous works by different teams, giving us the opportunity to work with some of the deepest imaging available and a wide variety of anciliarry data sets, including photometric imaging from HST & IRAC/Spitzer (Lotz et al. (2017)), wide field spectroscopy from MUSE/VLT (Richard et al. (2021)), multiple lens models (e.g, Bradač et al. (2009), Jauzac et al. (2014), Oguri (2010)) and photometric catalogs (i.e, Bradač et al. (2019), Castellano et al. (2016)).

The strong lensing effect produces a magnification on the high-redshift background galaxies that can range from a typical value of $\mu \sim 2$ over the full FOV of the HST images up to values of 20 or higher near critical lines. This enables the study of faint galaxies ($M_{1500} > -13$) that would only be reachable in blank field observations with much higher exposure times. Therefore, the MUSE data of these lensed fields gives us a window into some of the youngest and faintest LAEs and LBGs, but with only a fraction of the time and a comparable volume to that of blank field studies such as

the MUSE Hubble Ultra Deep Field[1], which has been previously used to, e.g., study faint LAEs and their involvement in the epoch of reionization (Hashimoto et al. (2017), Drake et al. (2017)).

1.5 About this Work

One of our main motivators is the work done by de La Vieuville et al. (2020), where they studied the intersection between the LAE and LBG populations at z$\sim$ 3-7 in Abell 2744. In their work they find *"No clear evidence for an intrinsic difference on the properties of the two populations selected as LBG and/or LAE."* through the methods that they applied, leaving some interesting questions open. We look to answer these questions with a different approach than de La Vieuville et al. (2020), by directly studying the Lyman-α emission line profile, the UV continuum, the UV slope, and the physical properties we can derive from SED fitting such as M_* and SFR.

Our work here focuses only in spectroscopic and photometric analysis of our sources. Another interesting approach for this study is the spatial extension of these high-redshift galaxies, especially the ones selected as LAE-LBG. We refrain from going further into this topic, as it involves more in-depth lensing analyses, and more importantly is being tackled by one of our collaborators (Claeyssen et al. in progress).

In this work, we will first present the data used for the three clusters Abell 370, Abell 2744 and MACS0416 in Section 2. In section 3 we explain the selection of pure LAEs, LAE-LBGs, pure LBGs and *Other LBGs*. We explain how we measured the parameters for the Lyman-α emission and UV continuum in Section 4. In Section, 5 we discuss our findings and their physical interpretations. Finally, we conclude our findings in Section 6, followed by an Appendix showing extra figures. For all measurements in this work, we adopt cosmological parameters Ω_M=0.3, Ω_Λ=0.7, H_0=70 km s^{-1} Mpc^{-1} and the AB magnitude system.

[1]http://muse-vlt.eu/science/udf/

Chapter 2

Data & Observations

For this work, we use data from the integral field spectrograph MUSE/VLT and legacy HST photometry from the Hubble Frontier Fields program. We study three strongly lensed clusters Abell 370 (z=0.375), Abell 2744 (z=0.308) and MACS0416 (z=0.396), the latter of these is separated into two different sections MACS0416N & MACS0416S. For the purpose of this work, we are particularly interested in the lensed sources behind these clusters. The most important of our data sets is the MUSE field spectra, with this we are able to directly identify LAEs and study their Lyman-α profiles over a large area, we then use HST data to complement and study the rest-frame UV continuum of these galaxies which is typically too faint to be detected by MUSE.

2.1 MUSE: Multi Unit Spectroscopic Explorer

The key dataset we use for this work comes from the integral field spectrograph MUSE/VLT. The observations were made using Wide Field Mode (WFM), with and without ground layer adaptative optics correction (AO and NOAO, respectively). The 1x1 arcmin^2 FOV of the WFM makes it possible to perform blind searches covering large fields, such as, Abell 370, Abell 2744 and MACS0416, with multiple adjacent pointings. The wavelength range of 4750–9350Å mixed with the 2–17 hour total exposure time and the wide lensed fields observed, let us study some of the faintest Lyman Alpha Emitters to date from $z\approx$2.9–6.7, reaching the borders of the reionization epoch. Thanks to the 1.25Å /pix spectral resolution of MUSE we are able to study the shape and properties of the Lyman-α profile of our targets. Exposure time is not homogeneous throughout the

field due to how the survey was constructed, some areas do have more exposure time than others due to different pointings, as show in Fig. 2.1 (taken from Richard et al. (2021)) and also in Table 3.1.

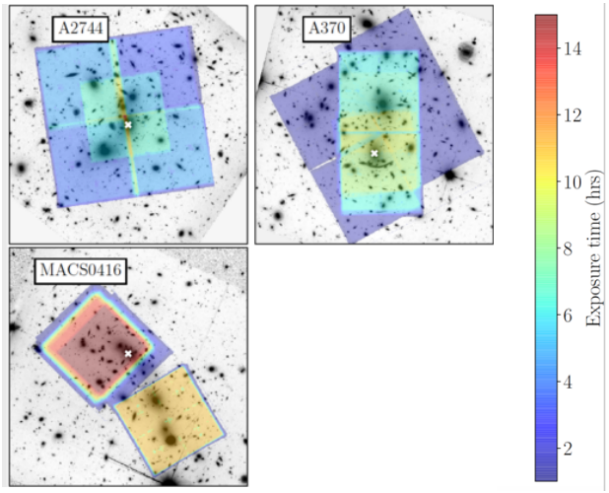

Figure 2.1: Pointings and exposure times for Abell370, Abell 2744, and MACS0416. This figure was taken from Richard et al. (2021). Further information can be found in Table 3.1.

The data reduction for this spectra was done by our collaboration as reported in Richard et al. (2021) with the MUSE Data Reduction Pipeline from ESO, following the procedure shown in Weilbacher et al. (2020) and the respective user manual[1].

2.2 HST: Hubble Space Telescope and Spitzer/IRAC

To supplement the data from the three strongly-lensed fields observed with MUSE, we use reduced images from The Hubble Space Telescope Frontier Fields program [2], designed by Lotz et al. (2014). This dataset consists in 3 images from F435W, F606W and F814W from ACS/HST and 4 images F105W, F125W, F140W and F160W from WFC3/HST (Koekemoer et al. (2014)) with a depth at 5σ of around $\sim$ 29 AB magnitude and 0.2" radius aperture. We used the final data version (v1.0) publicly available in the HFF website for each field, Abell 370, Abell 2744 and MACSJ0416.1+2403. The data from MUSE were spatially aligned to the HST images (see section 3.3), such that we can be confident that the photometry extracted can be matched to the Lyman-α

[1]https://www.eso.org/sci/software/pipelines/muse/

[2]https://archive.stsci.edu/prepds/frontier/

emission. We use the catalogs created by the AstroDeep team (Castellano et al. (2016), Merlin et al. (2016)). For objects in these catalogs, we are able to add photometry from the 3.6μm and 4.5μm filters of Spitzer/IRAC (Lotz et al. (2017)).

2.3 Lens models and multiple images:

The lens mass models used for the pure LAE and LAE-LBG sample were taken from Richard et al. (2010), Jauzac et al. (2015), and Jauzac et al. (2014) for the fields Abell370, Abell2744 and MACS0416, respectively, and were obtained via LENSTOOL. The high number of multiple image systems in these fields makes them a great target for obtaining accurate mass models of the lensing clusters, because of the strict constraints they provide over the models. Magnifications for pure LBGs were taken directly from the AstroDeep catalogs reported in Castellano et al. (2016). In Fig. 2.2, we show the magnification values for pure LBGs, pure LAEs, and LAE-LBGs.

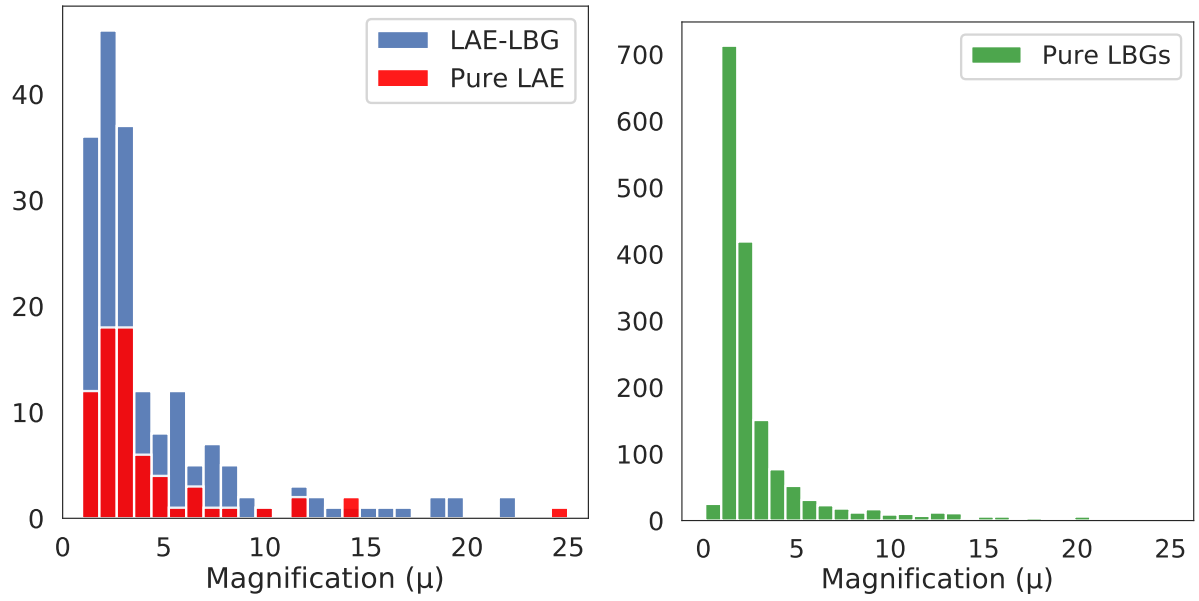

Figure 2.2: On the left magnificaiton results for both LAE selected samples. To the right magnification values for pure LBGs.

Chapter 3

Galaxy Selection

While the underlying star-forming population is thought to be a continuous population, spanning a broad range of properties, broad vs narrow band selection methods and sensitivities effectively split the SFGs into four distinct regimes, which we define as pure LAE, pure LBG, LAE-LBGs and other SFGs. We define a galaxy as a pure LAE when Lyman-α is detected in the MUSE cube, but no detection is observed in any of the 7 HST filters above the background. A pure LBG is defined as a source that is detected in the HST imaging, but does not have a Lyman-α emission present in the MUSE cube. LAE-LBGs, or the intersection between pure LAEs and pure LBGs, are defined as galaxies that are both detected by their rest-frame UV in their HST images and their Lyman-α emissions detected in the MUSE cube. Finally, we will refer to all other galaxies which do not show a Lyman Break or Lyman-α emission as other SFGs.

3.1 Initial Lyman Alpha Emitter Selection:

After reducing the MUSE cubes, we do an overall search of galaxies in the three fields. This procedure is explained in depth in Richard et al. (2021). Two different methods to search for galaxies are followed: first a search in the HST images of each field is done using *SExtractor* (Bertin & Arnouts (1996)) inside the FoV of the MUSE cubes, with the goal of searching for line emission (or other features) in the MUSE spectra. We call these: PRIOR sources. The second method consists in directly searching for line emission in the MUSE cubes, independent of the PRIOR sources found. For this purpose, *MPDAF* v2.0 (Piqueras et al. (2017)) is used to generate narrow-bands from the

Field	RA (J2000)	DEC (J2000)	z	Exposures [s]	Total exp. time [hrs]	Pure LAEs	LAE-LBGs	Pure LBGs	Other SFGs
Abell370	02:39:53.122	01:34:56.14	0.375	4×1800 (NOAO)	1.5-8.5	4	34	298	41
				37×962 (NOAO)					
				3×953 (NOAO)					
				24×930 (NOAO)					
Abell2744	00:14:20.702	30:24:00.63	0.308	40×1800 (NOAO)	3.5-7	34	97	342	215
MACS0416(N)	04:16:09.144	24:04:02.95	0.396	4×1800 (NOAO)	17	33	31	375*	203*
				27×1670 (AO)					
				6×1670 (NOAO)					
MACS0416(S)	04:16:09.144	24:04:02.95	0.396	50×700 (NOAO)	11-15	4	31	375*	203*
				8×667 (NOAO)					

∗: For MACS0416(N) + MACS0416(S)

Table 3.1: The three different fields studied in this work. MACS0416 was split into two different sections due to the surveys construction. Total exposition time varies, with MACS0416 overall having the most exposure. We can also see the number of galaxies found in each field by their detection regime. Each row corresponds to a different pointing.

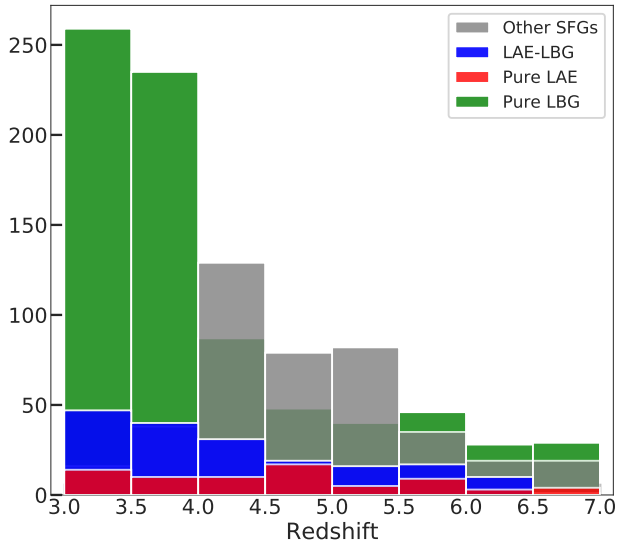

Figure 3.1: Redshift histogram for all sources presented in this work. We include redshifts from all confidence levels. The lack of *Other SFGs* at low redshift is due to the color criteria used, with a worse photometric coverage of the Lyman Break area at z~ 3-4.

MUSE cubes. The slices are then examined by *SExtractor* to find any line-emitting sources. We denote these as MUSELET sources. It is important to note that because HST imaging is much deeper than MUSE spectra, the PRIOR method allow us to push to lower S/N emission lines, which might not be detected by the MUSELET method. At the same time, MUSELET galaxies might

have very faint continua which are not detected in the PRIOR method, which is the case for the pure LAEs we find.

Once the initial galaxy extraction is ready, the spectral data are initially processed with the automatic redshifting software MARZ (Hinton et al. (2016)), which gives initial possible redshift configurations based on the presence of emission and absorption lines. Then, manual inspection is done by the different members of our collaboration on each source, we then do a final reconciliation between all members to discuss on the galaxies redshifts. For sources with tentative Lyman-α emission, secondary features are taken into account, such as additional emission & absorption lines, the presence of a Lyman break, spatial morphology and distortion due to strong lensing, the Lyman-α profile shape, continuum counterpart and color. In most cases, the only emission line that can be mislabeled as Lyman-α is the [OII]λ3727,3729, but the profile ratio and presence of secondary features are distinct enough that they can often be differentiated. We assign a confidence rating to the redshift of the sources: with 3 being very confident, with multiple spectral features; and 1 being less confident, with a single Lyman-α line. For this work we include galaxies from all confidence levels.

As mentioned in sec. 2.3, these fields contain many multiple image systems, among these are many of our sources. We find that 87 of our LAEs have 2 or more multiple images. For each system, only the image that has the strongest magnification, and therefore the one with the highest Lyman-α flux, is included, this way only the sources with the highest S/N are kept. With this change, the LAE sample size decreases from 417 to 268 sources.

3.2 Initial Lyman Break Galaxy Selection

For the initial selection of LBGs, we used the AstroDeep catalogs. We considered galaxies with photometric redshifts of $2.9 < z < 6.7$ to match with the redshift detection range of the MUSE data. We double check the photometric redshift of high-redshift AstroDeep sources, using BPZ, a bayesian photometric redshift analysis software (Benitez (2000)) which fits the AstroDeep photometry with a variety of different SED templates at $2 < z < 8$ with a resolution of $\Delta z = 0.05$ and a

flat prior. We kept candidates that have a $\chi^2 < 10.0$ in the BPZ results and a $z_{us} - z_{astrodeep} < 0.5$, where z_{BPZ} is the photometric redshift we obtained with BPZ and $z_{astrodeep}$ is the photometric redshift we found in the Astrodeep catalog.

After the photometric redshift selection, we perform a color criteria to separate the galaxies that show a Lyman Break to those who do not. We call galaxies that do not show a Lyman Break (nor Lyman-α) *Other SFGs*, and we find 459 of them.

We use the same color criteria to that of Bouwens et al. (2015) for z∼4-7 and J. Bouwens et al. (2016) for z∼3. For the z∼3 case we lack U336 data so the amount of pure LBGs will be overestimated in this redshift range. The color criteria selection used is:

$$z \sim 3 \quad : \quad F435W - F606W < 1.2 \quad \wedge \quad F814W - F105W < 0.7$$

$$\begin{aligned} z \sim 4 \quad : \quad & F435W - F606W > 1.0 \quad \wedge \quad F814W - F125W < 1.0 \quad \wedge \\ & F435W - F606W > 1.6 \cdot (F814W - F125W) + 1.0 \end{aligned}$$

$$\begin{aligned} z \sim 5 \quad : \quad & F606W - F814W > 1.3 \quad \wedge \quad F814W - F160W < 1.25 \quad \wedge \\ & F606W - F814W > 0.72 \cdot (F814W - F160W) + 1.3 \end{aligned}$$

$$\begin{aligned} z \sim 6 \quad : \quad & F814W - F125W > 0.8 \quad \wedge \quad F125W - F160W < 0.4 \quad \wedge \\ & F814W - F125W > 0.4 \cdot (F125W - F160W) + 0.8 \end{aligned}$$

$$\begin{aligned} z \sim 7 \quad : \quad & F814W - F125W > 2.2 \quad \wedge \quad F125W - F160W < 0.4 \quad \wedge \\ & F814W - F125W > 2.0 \cdot (F125W - F160W) + 2.2 \end{aligned}$$

3.3 LAE-LBGs and Pure LAEs:

After the initial LAE and LBG selections (see section 3.1 & 3.2), we want to further classify these galaxies as pure LAEs and LAE-LBGs. We astrometrically align the MUSE data cube to the corresponding HST imaging, with the goal to spatially match the Lyman-α emissions to their rest-frame UV continuum counterpart. In the case both of these quantities are detected, we define the object as a LAE-LBG. If the UV rest-frame is not detected, we then define them as pure LAEs. Through this method, 193 galaxies compose the LAE-LBG sample and 75 galaxies the pure LAE sample. All LAEs sources published in this work were visually inspected to ensure that the UV detection is reliable and LAEs are accurately labeled as LAE-LBGs or pure LAEs. The redshift distribution for LAE-LBGs and pure LAEs is shown in Fig. 3.1.

3.4 Pure LBGs and Crossmatching

To clean our Pure LBG selection of LAEs, we perform a cross-match between our LAEs and the LBGs found in Sec. 3.2. Considering the Lyman-α emission can be more diffuse than the UV emission, sometimes forming a halo around the galaxy, crossmatching the MUSE data to the HST data may be inaccurate. To reduce false positives, we discard all galaxies present in our initial LBG selection (see Sec. 3.2) that are within 0.5" of a LAE. Through these method we achieve a total of 1015 pure LBGs between Abell 370, Abell 2744 and MACS0416 (See Table 4.1 and Table 3.1).

3.5 Upper Limits

Given the observations of the Hubble Frontier Fields for the 3 ACS/HRC and 4 WFC3/IR bands, it is possible to establish upper limits on the photometry for each pure LAE to better constrain the properties of our sample. We note that upper limits will not be uniform due to the large number of foreground galaxies across the observed area. For this purpose, we define the detection limit at 3σ.

We calculate σ directly from the flux distribution centered at the galaxy's coordinates within an aperture of r = 0.25″ (see Fig. 3.2). Physically this radius corresponds to r = 1.85–1.45 kpc, which

ACS/HRC			WFC3/IR			
F435W	F606W	F814W	F105W	F125W	F140W	F160W
25.665	26.493	25.947	26.2687	26.2303	26.4524	25.9463

Table 3.2: Zero points for the 3 ACS/HRC and 4 WFC3/IR filters, in AB magnitude for an infinite aperture.

should be sufficient to contain a high-redshift galaxy candidate which has a typical intrinsic radius 0.15–0.8 kpc (Kawamata et al. (2015)). For more extended sources, with higher magnifications, they will be somewhat underestimated, but regularly the UV continuum emission of LAEs is much more compact than Lyman-α, due to the lack of resonant scattering processes.

$$m_{AB,lim} = -2.5 \cdot log_{10}(N_{pix}(\mu + 3\sigma)) + zpt \tag{3.1}$$

The limiting magnitude then is defined as in eq. 3.1, with μ being the mean value of the counts within the aperture, and zpt the zeropoint of each filter in the AB magnitude system. The values for the photometric zero points are given in Table 3.2. We define the term N_{pix} as the minimum number of pixels above the 3σ threshold that are needed for a detection, we set this constant to a general value of 10 pixels, following the *SExtractor* parameters used in Richard et al. (2021) to measure the photometry for our LAEs.

As we already mentioned, one of the key factors for the determination of the limiting magnitude is the immediate vicinity of a foreground galaxy. We can expect lower limiting magnitudes in regions that are contaminated by other sources, while regions that have no contamination will have higher limits. We can see a typical example of this in Fig.3.2, the upper limit can vary several magnitudes depending on the state of the background. We see an example of this in LAEs ID:M230 and ID:M203, the contamination affects the value by a factor of $\sim$ 3 magnitudes.

Taking into account the 7 filters, $\sim$ 87 % of pure LAEs suffer low to no background contamination, with an upper limit of $m_{AB} > 28.5$ in all filters, while the rest suffers from stronger contamination similar to LAE ID:M203. We show the limits of all filters combined in Fig.3.3.

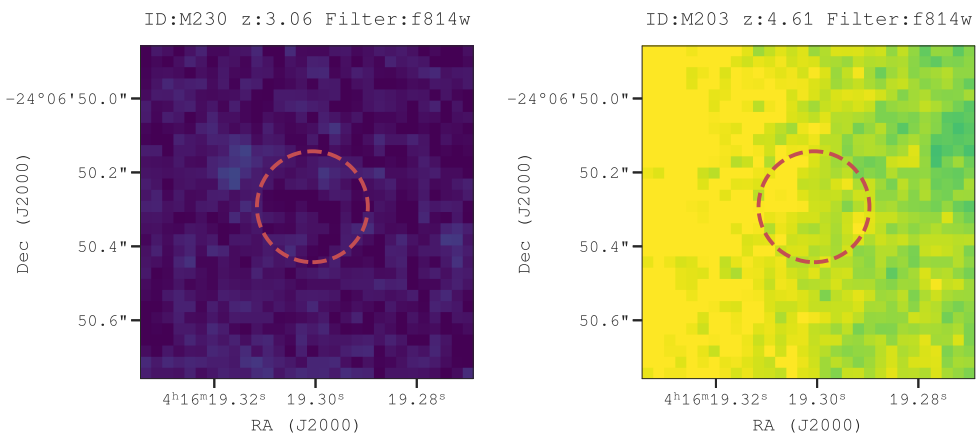

Figure 3.2: Non-detection rest-frame UV images of two pure LAEs. To the left is LAE ID:M230 with no contamination and an upper limit of $m_{F814W,AB} > 30.4$. To the right is LAE ID:M203 which is contaminated by a background source and has an upper limit of $m_{F814W,AB} > 27.6$.

For pure LBGs, and *Other SFGs*, we set a constant upper limit value, taking the flux which encloses 90 % of the Lyman-α detections in the MUSE data, this value ranges from 0.1 to 0.33 $erg/s/cm^2$ depending on the exposure time of each field, and is then scaled according to the magnification value of each galaxy.

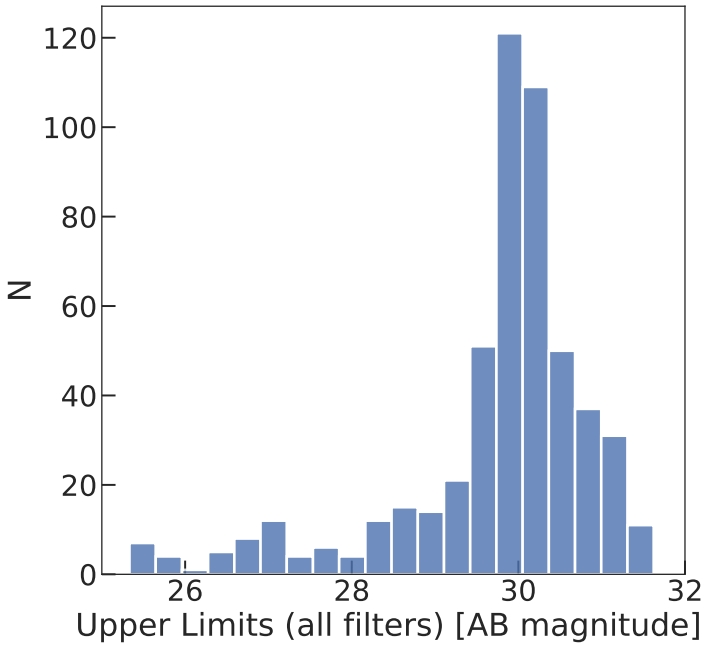

Figure 3.3: Upper limits obtained for the 7 HST filters. Each upper limit for each filter is shown. Only ~13% of sources have a strong contamination, resulting in upper limit of $m_{AB} < 28.5$.

Chapter 4

Continuum and Emission Line Parameter Estimations

In this section we explain the properties we studied for our galaxies, the features we focused on are their Lyman-α emission observed with MUSE and its profile shape, and the UV rest frame continuum observed with the HST from which we can derive star formation rate and stellar mass.

4.1 Lyman-α Luminosity and UV Absolute Magnitude

For the pure LAE and LAE-LBG samples, we initially extracted the Lyman-α flux from the MUSE spectra by fitting a Gaussian profile to the data. This proved to be sufficient for a limited portion of the sample, but due to the distinct non-Gaussian shape that the Lyman-α line can take, we individually inspected the spectra of each source to set the extraction limits. When there is presence of continuum from the source or from foreground galaxies, we take the flux points outside the extraction limits in a range of 50Å in both wavelengths sides and perform a linear fit, we then subtract this continuum from the spectra. The flux was then transformed to its corresponding luminosity value:

$$L_{Ly\alpha} = \frac{f}{4\pi Dl^2}/\mu \quad [erg/cm^2/s] \tag{4.1}$$

Where f is flux, μ the magnification factor and Dl the luminosity distance given the z_{spec} obtained from Lyman-α or the systemic redshift obtained from other complementary lines such as

CIVλ1549, CIII]λ1909 or rarely absorption features. We also correct by magnification using the lens models constructed by Richard et al. (2021).

For the populations of LAE-LBG, pure LBGs, and *Other SFGs*, we use the photometry described in section 2.2 to obtain the absolute UV magnitude. To have a standard measurement within our sample and for ease of comparison with the literature, we calculate the absolute magnitude from the rest-frame UV continuum 1500Å . We consider the UV continuum as a power law $F_\lambda = C \cdot \lambda^\beta$ and perform a fit accordingly, using the HST data of the 7 filters already described. In case that a band is contaminated by the Lyman-Break, we discard it. We take into account the contribution of the Lyman-α line on the continuum measured by the HST imaging, and subtract it according to the flux calculated from the MUSE spectra. Then we convert to absolute magnitude:

$$M_{1500} = m_{ap} - 5(log_{10}(Dl) - 1) \tag{4.2}$$

$$m_{ap} = -2.5 \cdot log_{10}(f/(1+z)/\mu) - 48.6, \tag{4.3}$$

where M_{1500} is the absolute magnitude at rest-frame 1500 Å and m_{ap} is the AB apparent magnitude at 1500 Å. We do not correct M_{1500} for dust extinction.

Results for these measurements are shown in Fig. 4.1, where we differentiate the three populations of galaxies by the different colors.

4.2 Lyman-α Profile:

With the 1.25 Å /pix spectral resolution of MUSE, we were able to directly study the Lyman-α profile. Due to the highly asymmetric profile of Lyman-α, it is normally described as a multi-Gaussian function, this makes it highly dependant on the χ^2 value or goodness of the fit. To avoid this, we opt for a non-parametric approach when doing our analysis. The spectral resolution of MUSE is enough so that we can distinguish different structures and types of asymmetry in each Lyman-α profile, such as the presence of the blue peak or lack of it.

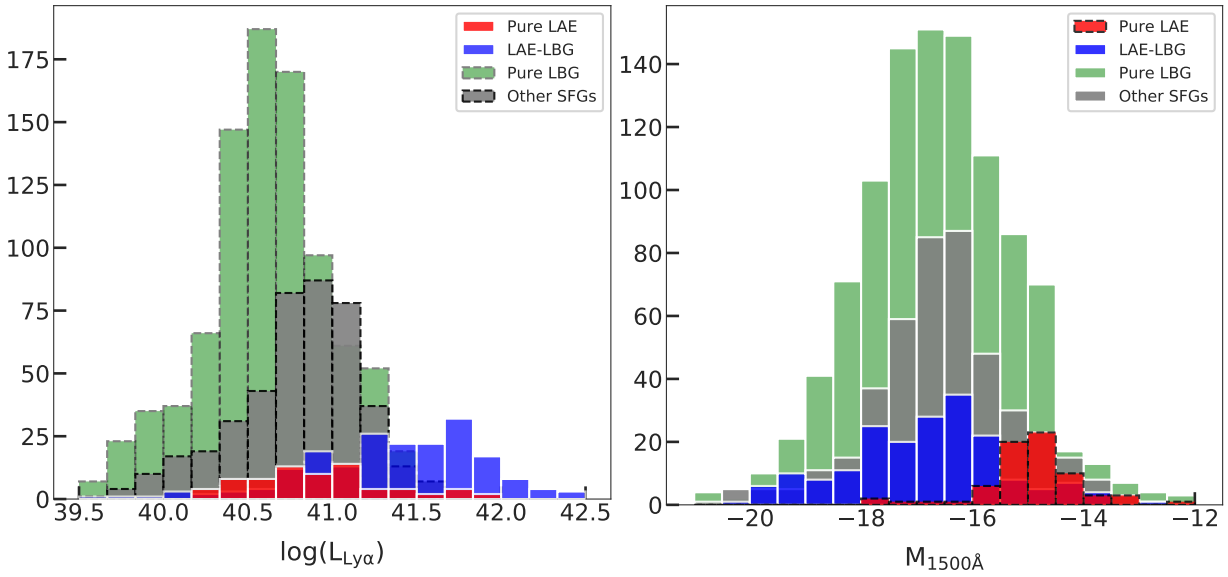

Figure 4.1: We present the results for Lyman-α luminosity (Left) and UV absolute magnitude at 1500 Å (Right). We show pure LAEs (Red), LAE-LBGs (Blue), pure LBGs (green) and *other SFGs* (gray). Dashed black lines show when upper limits are used.

To study both the broadness and asymmetry, a non-parametric percentile method was used. Through this method, we can better differentiate between different Lyman-α profile shapes by re-binning the spectra from 1.25Å to 0.1Åwith a linear interpolation, in order to alter the original data the minimum necessary. To define the edges of the line wings we initially approximated them using a Gaussian fit (edge would be defined at 3σ) and then refined the edges through individual inspection, taking into consideration both blue and red peaks when relevant. To give a quantitative measurement of asymmetry we calculate the difference between the peak of the Lyman-α profile and its 50th percentile ($\lambda_{50th} - \lambda_{peak}$); symmetric profiles (e.g. single Gaussian) will yield a value of 0, while positive values imply a more red-heavy profile, and negative values imply a blue-heavy profile. To study the average profile types of our galaxy sample we divide our LAEs into 4 quartiles with respect to their asymmetry values and build composite spectra of each quartile. Results for this test are shown in Fig. 4.3, where negative values (blue-heavy profiles) tend to have a stronger blue peak component while positive values (red-heavy profiles) lack this feature. To obtain a non-parametric estimate of the velocity width of our galaxies we again used a percentile approach, taking the wavelength difference of the 40th and 60th percentiles in order to

obtain the broadness of the emission line. We chose this percentile ranges to avoid weighting too much the wings of the profiles in low S/N sources, which would add more noise to the measurement.

We also perform equivalent width (EW) measurements of Lyman-α, we do this to understand how strong the emission line is compared to the galaxies continuum. We take the ratio between the flux of Lyman-α and the mean flux of the UV continuum between 1228 Å and 1255 Å ,taken from the best-fit of the HST photometry similar to how M_{1500} was obtained in Sec. 4.1. We do not take the flux of wavelengths lower than Lyman-α to avoid contamination due to the Lyman Break. In the case of pure LBGs we do the same but replace the Lyman-α flux for the limiting flux (0.1 to 0.33 $erg/s/cm^2$) we define in Sec. 3.5. For pure LAEs we can follow the same procedure and use their UV continuum upper limits to constrain their EW.

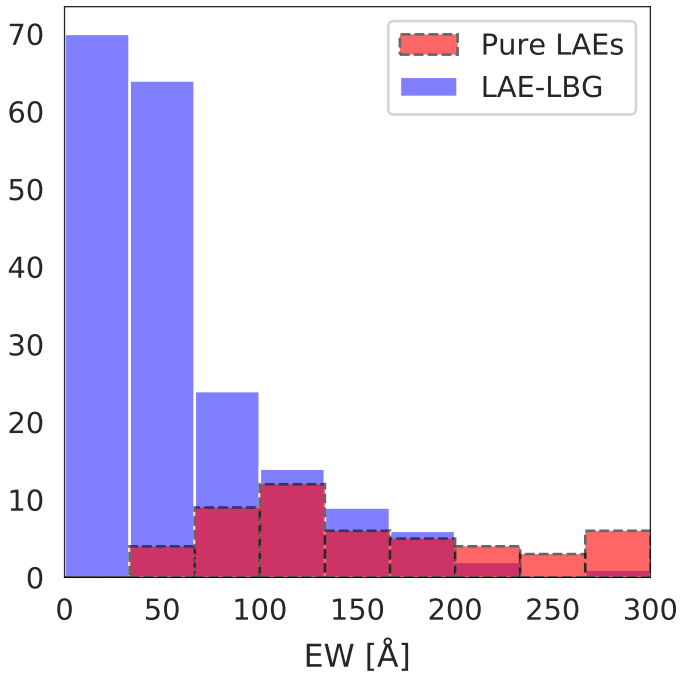

Figure 4.2: Equivalent width for LAE-LBGs (green) and pure LAEs (red). Pure LAEs EW values are upperlimits. By definition there is a lack of pure LAEs with low EW, since we don't have directi detections of their UV continuum.

The non-parametric approach we applied in the last paragraph does not let us obtain error-bars

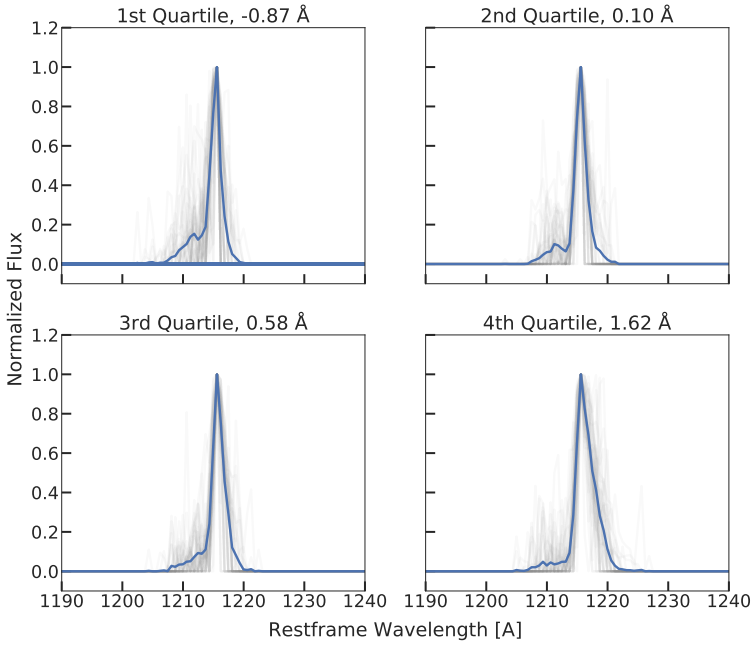

Figure 4.3: Combined Lyman-α profiles for the first to fourth quartiles of asymmetry values. All fluxes were normalized, matched by the peaks and summed up. There is clear evolution of the blue peak from the 1st to the 4th quartile.

directly from the data (shown in 5.9). For this task, we used a simple Monte Carlo method, taking the baseline variance error for our spectra outside the Lyman-α line wavelength, calculating its 1σ error and applying a Gaussian error to our data based on these parameters. We then added Gaussian errors based on these parameters to each of the Lyman-α profiles, doing 100 iterations for each galaxy. From these new asymmetry and broadness results, we took the 1σ errors shown in Fig. 5.9.

4.3 UV Slope

We estimated the UV slope from the photometric data points obtained from the HST bands. The procedure followed was similar to that of section 4.1 where M_{1500} was calculated, but this time we focus on the value of the slope of the fit, which we then transform into the β slope parameter as $f_\lambda \propto \lambda^\beta$. Again, we don't consider filters that may be contaminated by the Lyman break and as before we deduct the Lyman-α flux. Results are shown in Fig.5.3, where we clearly find that both populations have a significant difference on their distributions, with pure LBGs having a median slope of β=-1.75, LAE-LBGs a median slope of β=-2.44 and *other SFGs* a median of β=-1.59 (see

Table 4.1).

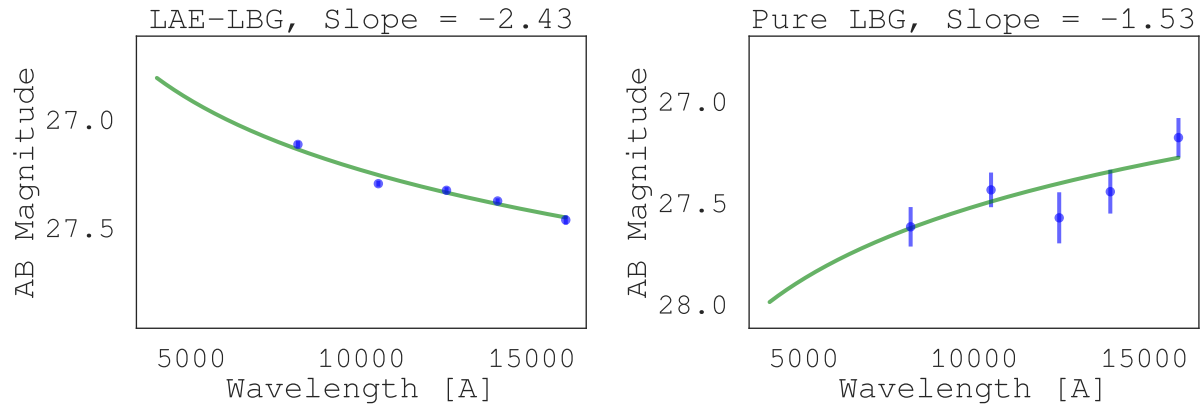

Figure 4.4: Examples of the best-fit slopes for a typical LAE-LBG z=3.87 (left) and pure LBG z=3.28 (right). The green line shows the best-fit $\log(F_\lambda) = \beta\lambda + C$. The β values are shown on top, and are near the calculated medians for the distributions shown on Fig. 5.3. Slope uncertanties are calculated from the covariance of the fit, given the photometry errors.

4.4 Physical Properties

Using the HST continuum observations from Sec. 2.2, we estimate the physical properties of the galaxies with the SED fitting code iSEDfit[1] published by Moustakas (2017). iSEDfit uses the stellar population synthesis method (SPS), where galaxies are built from different stellar populations based on the different prior parameter distributions we input. Since we accurately know the spectroscopic redshift of LAE-LBGs, we establish a fixed value for redshift. In the case of pure LBGs, we set the redshift as the value given by the AstroDeep catalogs. For the SPS galaxy modelling we follow the recommendation of the iSEDfit documentation, using the FSPS v2.4 routine (Conroy & Gunn (2010)), the stellar libraries from MILES+BaSeL (Sánchez-Blázquez et al. (2006), the Chabrier (2003) IMF, Padova (2009) isochrones, and the reddening curve defined by Charlot & Fall (2000). Finally, we considered a delayed star formation history model, with prior uniform distributions of τ = [0.001,3.0] Gyr and age = [0.1,3.0] Gyr. We define a uniform prior distribution for stellar metallicity

[1]https://github.com/moustakas/impro

Z = [0.0008,0.03] according to the recommended configurations. With these properties, 20,000 different SED models are made with Monte Carlo grids, it is possible to increase this to around 100,000 models, but the quality of the results does not change significantly for the required computation time.

With the different models and Bayesian statistics, iSEDfit returns multiple physical properties, the most interesting for this work being, star formation rate and stellar mass (M_*). We do not report values of galaxies with poor χ^2 values or lack of data in the resulting posterior distributions.

Results are shown in Fig.4.5 and Fig. 5.8, where we compare LAE-LBGs to pure LBGs and *other SFGs*, it is important to note that the stellar masses calculated for pure LBGs and *other SFGs* are expected to be more accurate due to the extra IRAC/Spitzer data provided by the AstroDeep catalogs.

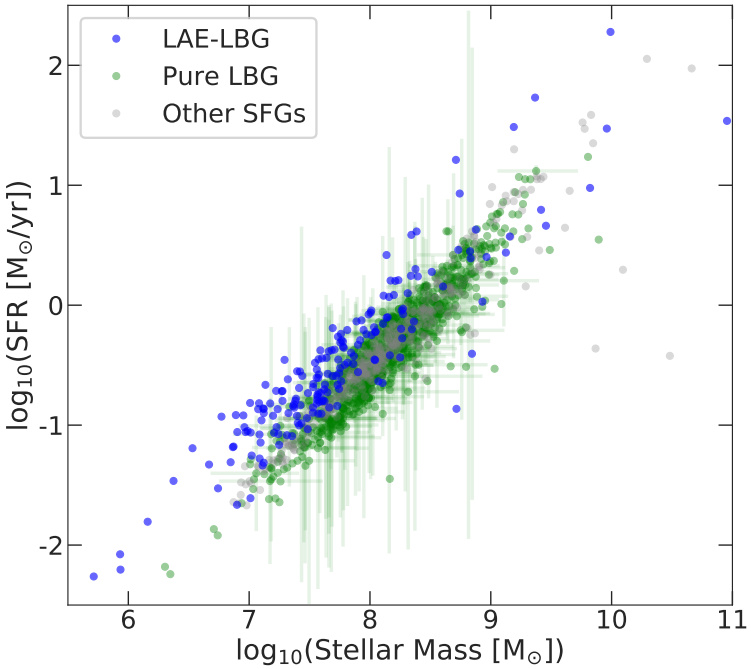

Figure 4.5: The main sequence for LAE-LBGs (blue), pure LBGs (green) and *other SFGs* (gray), 1σ error bars are shown for only half of the sources. Comparison between the star formation rate and stellar mass. We see at first glance that both populations are shifted, which would indicate that overall, LAE-LBGs tend to have stronger SFRs for a given stellar mass. This trend is more pronounced at lower stellar masses and is also related to redshift as we will discuss.

Population	Number of Sources	Asymmetry [$\mathring{A}$]	Broadness[km/s]	UV slope [β]	EW[$\mathring{A}$]	sSFR [Gyr^{-1}]
Pure LAE	73	0.21	47.84	-	-	-
LAE-LBG	193	0.38	66.43	-2.44	42.72	6.06
Pure LBG	1015	-	-	-1.75	< 9.7*	2.88
Other SFGs	459	-	-	-1.59	< 17.79*	3.16

$*$: Upperlimit

Table 4.1: Results for the four populations of interest. We show dashed values it was not possible to make a measurement do to the characteristics of the population.

Chapter 5

Results and Discussion

In the next section we discuss our findings concerning the Lyman-α profile and UV continuum of pure LAEs, pure LBGs, LAE-LBGs, and *other SFGs*, according to our findings and the literature.

5.1 Lyman-α and UV emissions

With the results from Sec. 4.1 we now study the relation between Lyman-α and the UV continuum, through their luminosity and absolute UV magnitude at 1500 Å respectively. As shown in Fig. 5.1, we see clear trends for each population, as we might expect considering that Lyman-α emission is photoionized by the UV continuum from massive young stars. While both emissions are a byproduct of young stars, the UV continuum is directly emitted from these, while Lyman-α will be produced from the HI gas previously excited by the ionizing radiation of the star. Therefore, even if both emissions are similar in their root of origin - young stars - the mechanisms that rule over their radiative transfer are not. While both of them are affected by the interstellar dust, Lyman-α in particular is susceptible to neutral hydrogen, causing absorption and resonant scattering in the ISM and absorption in the IGM, but this second effect is only noticeable at redshifts higher than z$\sim$ 7 (i.e. the epoch of reionization).

Notably, the star-forming populations in Fig. 5.1 span at least $\sim$ 2 dex in $L_{Ly\alpha}$ and several magnitudes in M_{1500A} for any fixed value in the other parameter, showing a wide diversity of combinations for both emissions. This translates into a difference in the star formation trend shown in Fig.

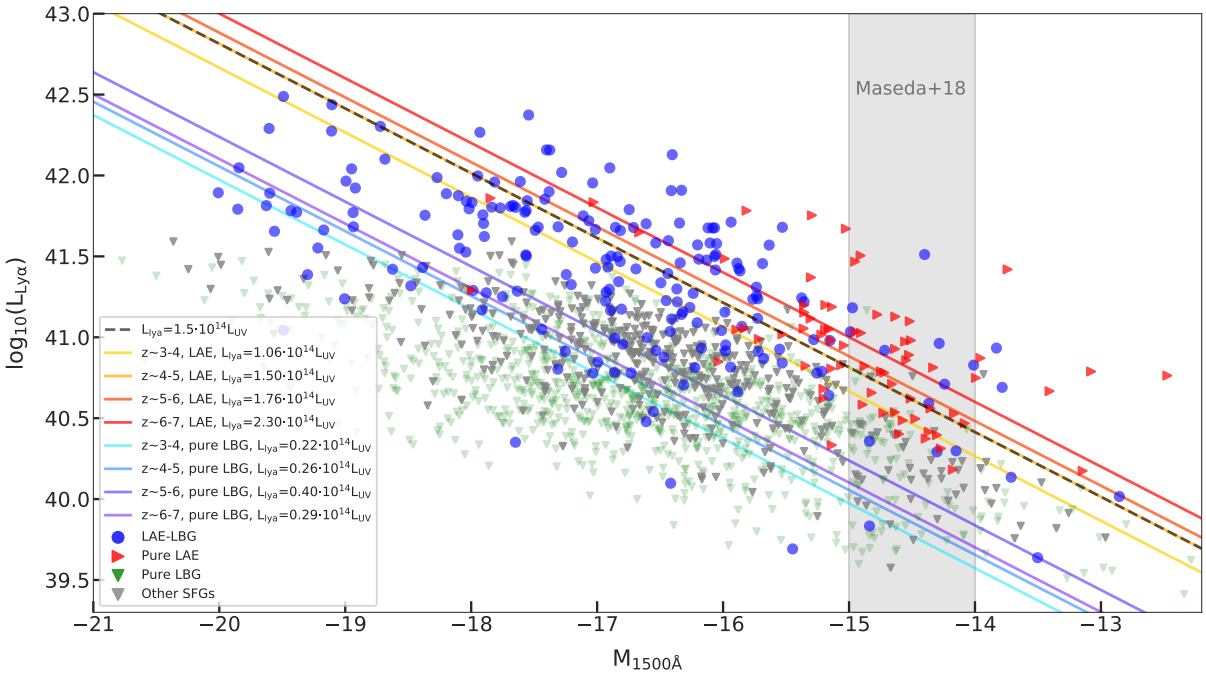

Figure 5.1: Comparison between Lyman-α luminosity and absolute magnitude UV measured at 1500 Å for galaxies studied in this work. We show LAE-LBGs (blue), pure LAEs in red (right-facing triangles denoting lower limits in M_{1500}), pure LBGs in green and *other SFGs* in gray (down-facing triangles denoting upper limits in $\log(L_{Ly-\alpha})$). In a gray area we show the range of M_{UV} values obtained by Maseda et al. (2018) for pure LAEs by stacking HST images for galaxies with $\log(L_{Ly\alpha})$ = 40.8 - 42.5. The dashed black line is the relation for constant star formation $SFR_{Ly\alpha}$ = SFR_{UV}. The solid colored lines represent the same star formation relation as best-fit to the pure LAE and pure LBG samples assuming a fixed slopes of unity for bins of Δz=1, with the lines colored from cyan to purple being redshift ranges for pure LBGs (from low to high redshift) and yellow to red for LAEs. Galaxies with extreme values (i.e. M_{1500}>-13) are due to high magnifications near the critical lines of the lensing models.

5.1, with a big offset of ~1 dex (see labels Fig. 5.1) between LAEs and pure LBGs (and *other SFGs*) at every redshift. Important to note that we work with a fixed slope of 1, but the data shown might suggest a different slope, we fix it to unity because two of the populations are only upper limits. Also, from these star formation trends, there appears to be a correlation with redshift especially for LAEs, with galaxies in high redshift bins having higher $SFR_{Ly\alpha}$ (compared to SFR_{UV}). Although this might be biased, because of the fact that it is easier to detect bright high-redshift galaxies than fainter ones, this bias is more clear for the pure LBG population of Fig. 5.2. From this we can

also say that Lyman-α is not as reliable an indicator of star formation rate as observing the UV continuum directly, due to its propagation and interactions with HI, as well as the dust obscuration which affects both Lyman-α and the continuum.

In Fig. 5.1, we find an absence of galaxies with high Lyman-α luminosity at high UV magnitudes (above the constant star formation line at M_{1500}>-18). One of the possible reasons for this effect is that galaxies with high masses, corresponding to M_{1500}>-18, also have large amounts of dust as a byproduct of star formation, and therefore it might not be possible to observe Lyman-α due to the dust absorption. We will revisit this topic later when discussing the UV slope of our sources.

The radiative transfer of Lyman-α is a complex topic, and involves the many variables listed during our introduction, therefore an answer for the lack of Lyman-α emission in pure LBGs and *other SFGs* will not come from a singular source. The considerable scatter of almost 2dex we find for Lyman-α vs M_{1500} in Fig. 5.1 is due to Lyman-α being not only sensitive to the dust produced in star-formation, but also to the HI resonant scattering, which scatters Lyman-α photons out of the LOS, sometimes producing extended and diffuse emissions around the star-forming regions. Following this, we could expect galaxies that have a dust-obscured UV continuum blocked in the LOS to be visible in Lyman-α due to the sometimes extended Lyman-α halo, which would let this emission escape towards our LoS through different angles (Leclercq et al. (2017)). We will revisit this discussion in Sec. 5.2 and Sec. 5.4.

We also find a lack of pure LAEs with high Lyman-α luminosity ($\log(L_{ly\alpha})$>42.0) at faint UV absolute magnitudes. This very likely implies that there is a physical limit bounded by the 1:1 SFR trend line (accounting for dispersion). A galaxy does not appear to have strong Lyman-α without sufficient UV continuum that photoionizes the hydrogen. Nonetheless, we find most pure LAEs near the 1:1 limit. Since we only have upper limits for their UV detections, the question of what is the true value of $M_{1500\text{Å}}$ for pure LAEs and how their strong Lyman-α emission is powered still stands. One way to retrieve the undetected UV continuum emission of pure LAEs is to stack the HST images of different galaxies to get a detection. Since we are working on highly lensed fields, this process is not straightforward to implement due to the different ranges of magnifications. Instead,

we plot in Fig. 5.1 the results of pure LAE stacking by Maseda et al. (2018) in the UDF (*Ultra Deep Fields*) blank fields. They report values between $M_{1500Å} \sim -15 - -14$ for Lyman-α luminosities between $10^{40.8}$ and $10^{42.5}$ erg s^{-1}. These values seem consistent with our results, although we rich lower Lyman-α luminosities than their team, probably due to the lack of lensing factor in the UDF.

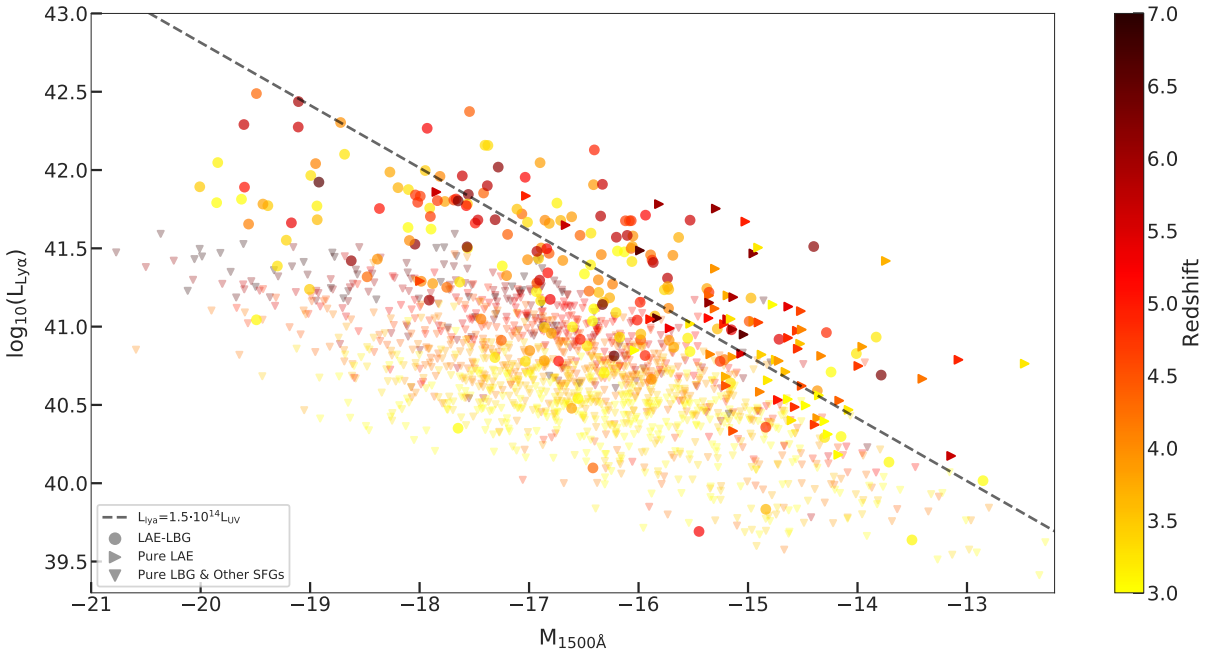

Figure 5.2: Similar to Fig. 5.1. We show redshift as color. There is no clear overall trend with redshift. For pure LBGs we see some form of Malmquist bias, with an over representation of bright high-redshift galaxies.

5.2 Lyman-α and the UV Slope

One of the main sources of the extinction of the UV continuum in star-forming galaxies is absorption by dust. This dust will be heated, and then emit thermally in the far infrared. It is also expected that UV photons have a higher absorption cross section by the dust. Due to this, and as seen in Fig. 5.3, objects that have a higher abundance of dust, will also have overall redder UV slopes (greater value of β), compared to a galaxy with a dust-free environment which will have a stronger FUV component and therefore result in more negative β values.

We find evidence in Fig. 5.3 that overall pure LBGs and *other SFGs*, have redder UV slopes of β=−1.75 and β=−1.59. This could imply greater ages and more reddening due to the present of dust, compared to LAE-LBGs, which show bluer UV slopes with a median value of β=−2.44. Most of the LAE-LBGs are near the dust-free domain of $\beta \lessapprox -2.4$. This clear difference in UV slope between the populations implies that the dust produced from stellar processes is an important factor in the lack of observable Lyman-α lines in pure LBGs. Another possibility is that pure LBGs are slightly older and their stronger younger populations of stars has already died out. We also find a subset of pure LBGs which show a low extinction environment and LAE-LBGs which show high extinction, this implies that dust is not the only cause for the lack or presence of Lyman-α, and other factors such as the line of sight to the galaxy, the gas kinematics, its column density and distribution also play fundamental roles. For example, a particular LOS to the star-forming regions in a dust-rich galaxy might let Lyman-α escape and be detected by the observers, while conversely a particular LOS in a dust-poor environment might not let Lyman-α escape to the observers. This could lead to greater dispersion between the observed $L_{Ly\alpha}$ and L_{UV} measurements.

In Fig. 5.4 we show UV slope on the Lyman-α UV absolute magnitude plane. Again there is a strong separation between LAE-LBGs, pure LBGs and *Other SFGs* and we can see a clear change in the UV slope with Lyman-α luminosity, from -1.58 at $39.5 < \log_{10}(L_{Ly-\alpha}) < 40.0$ to -2.22 at $42.0 < \log_{10}(L_{Ly-\alpha}) < 42.5$. This correlation between UV slope and $L_{Ly\alpha}$ is not as clear when we study individual populations separately.

Taking the previous into consideration, it is clear that overall LAE-LBG tend to be more dust-free and/or older than pure LBGs and *Other SFGs*, although with a significant overlap for values below $\beta < 1.5$. Nonetheless, the bulk of LAE-LBGs are even bluer than typical reported dust-free configurations: e.g. β=-2.25 Calzetti (2001) and β=-2.23 Meurer et al. (1999), which implies a very metal-poor young stellar population. All of this agrees with the fact that high-redshift galaxies tend to have lower metallicities (Maiolino et al. (2008)) than local sources and stronger sSFRs (Khochfar & Silk (2010)).

The differences found between the UV slopes of pure LBGs and *Other SFGs* shows that the

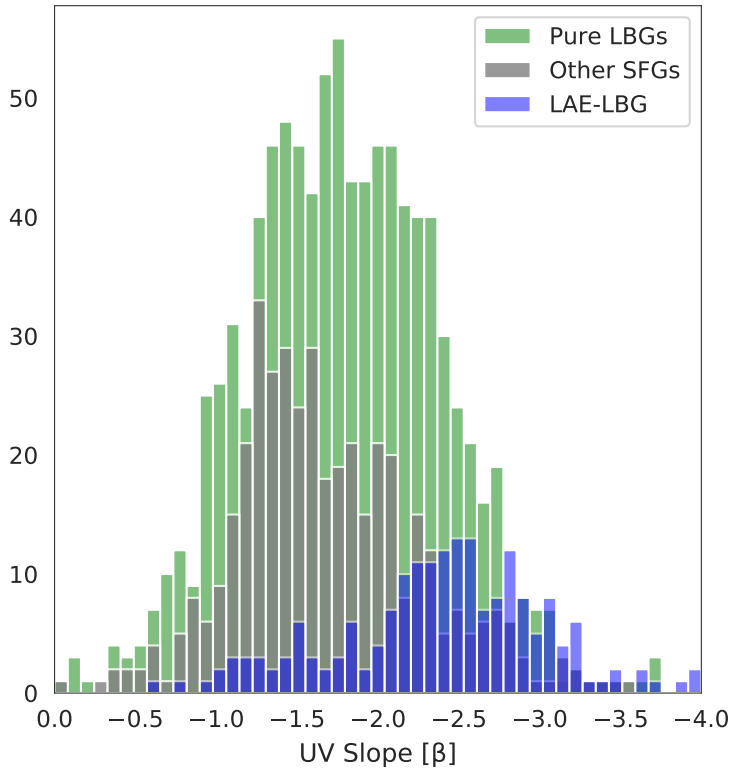

Figure 5.3: Comparison between UV slopes of pure LBG (red), LAE-LBG (blue) and *Other SFGs* (gray). There is overlap between populations but the distributions are clearly centered differently with a difference of $\Delta\beta \sim 1$. Extreme cases (i.e. $\beta \sim -4$) are due to unreliable photometry and present large errors.

former regime tends to have bluer UV slopes. This can be explained by the color criteria selection of pure LBGs favoring sources which have stronger UV slopes which also tend to be bluer. Nonetheless, we can conclude that galaxies that are not Lyman Break selected tend to have redder UV slopes, due to a higher dust extinction or older stellar populations.

In Fig. 5.5 we compare the extinction parameter A_v to the UV slope. We can see a correlation between the two parameters, which corroborates the idea that pure LBGs and *Other SFGs* tend to have a stronger dust extinction, resulting in a redder UV slope. Nonetheless, we cannot easily isolate the two factors that dictate the UV slope, since it depends on both the dust absorption and the age

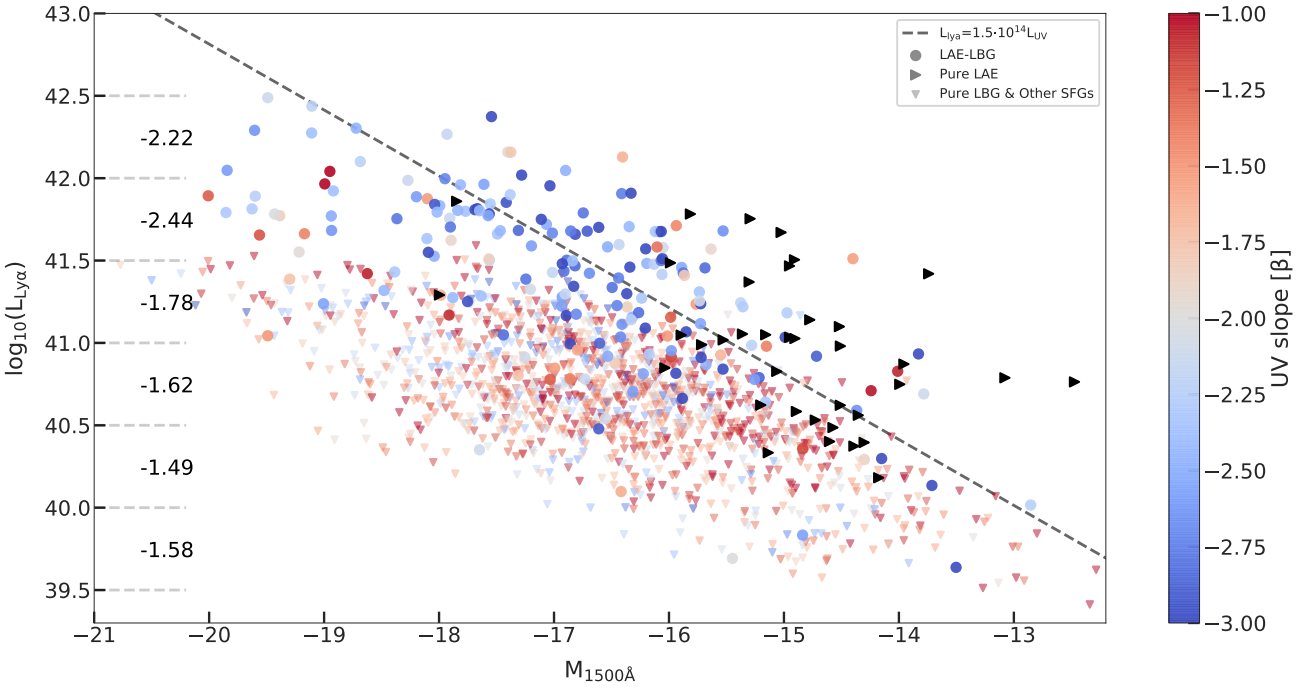

Figure 5.4: Similar to Fig. 5.1 but with UV slope as the colorbar. Bluer colors show bluer (more negative) UV slope β values, while redder colors show higher and redder slopes. Pure LAEs are shown in black since no UV slope was measured. Clear distinction between the regimes with LAE-LBGs being much bluer. We show to the right of the Y-axis, UV slope median values grouped in Δ=0.5 bins of $\log_{10}$(LLya) for the combination of pure LBGs and LAE-LBGs.

of the galaxy. Older galaxies have older stellar populations which have less young stars, producing a redder UV slope, changing β in a similar way to that of the dust attenuation. We can see this in Fig. 5.6, where age and β follows a similar trend to that of Fig. 5.5, where the older pure LBGs tend to have redder UV slopes. Please note that the age results for LAELBGs in Fig. 5.6, may not be accurate due to a lack of IRAC/Spitzer data from the older stellar populations. However, the correlation still stands if we remove LAELBGs from this plot. No remarkable differences is found between pure LBGs and *Other SFGs* for A_v and age.

An interesting note about Fig. 5.5: in the same figure we see a couple LAELBG outliers with high A_v and a red UV slopes, all of them have a detected Lyman-α profile even for their heavily obscured UV continua. Given the correct morphology, this may be explained by a strong Lyman-α

halo that propagates the emission to our LoS due to resonant scattering, while the compact UV continuum of the galaxy is obscured. A proper spatial analysis of the sources is needed to confirm this.

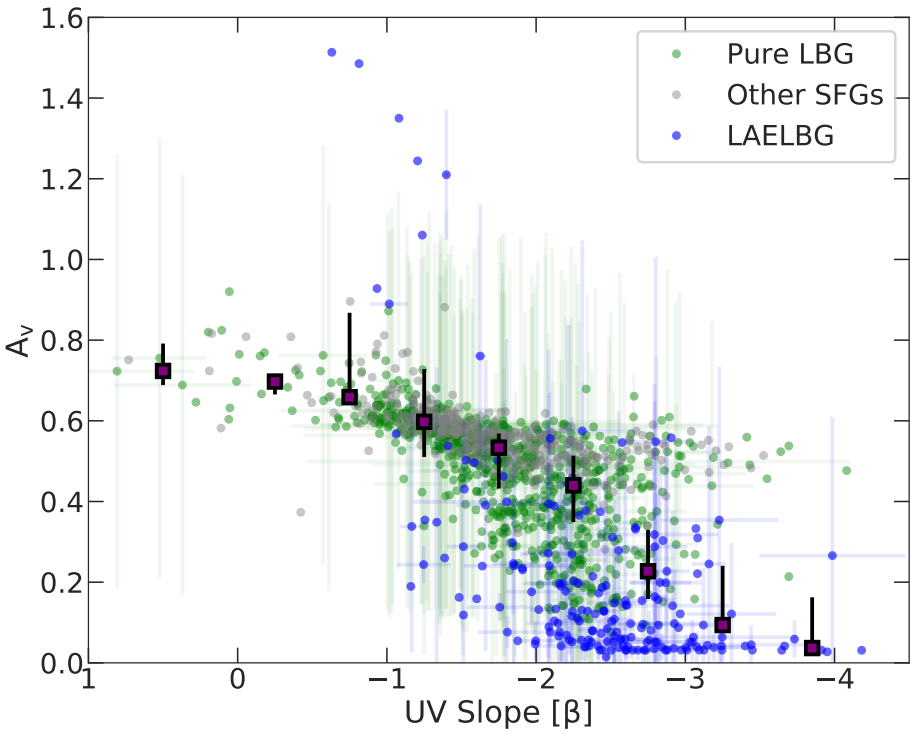

Figure 5.5: We show pure LBGs (green), LAELBGs(blue) and *Other SFGs* gray. In purple with black contours are the median values for bins of $\Delta\beta$ = 0.5. To weight both populations equally, we take random pure LBGs equal to the number of LAELBGs. We find a correlation between both parameters, confirming that pure LBGs tend to be more dust obscured. We also find high A_v, high β LAELBG outliers, which may be explained by a diffuse Lyman-α halo with an obscured and compact UV continuum.

Another way we can study Lyman-α is by comparing its strength or EW with the UV slope. In Fig. 5.7 we can see, with a significant dispersion, that, as expected, the galaxies with the highest EWs tend to have negative β values. Nonetheless, we find a considerable amount of pure LBGs with less negative slopes and 10Å <EW<100Å this implies that these galaxies are heavily obscured by dust, preventing us from detecting their Lyman-α emission. As expected, we find almost no dust-free galaxies with low EWs, since a dust-free ISM makes it easier for Lyman-α to escape. We

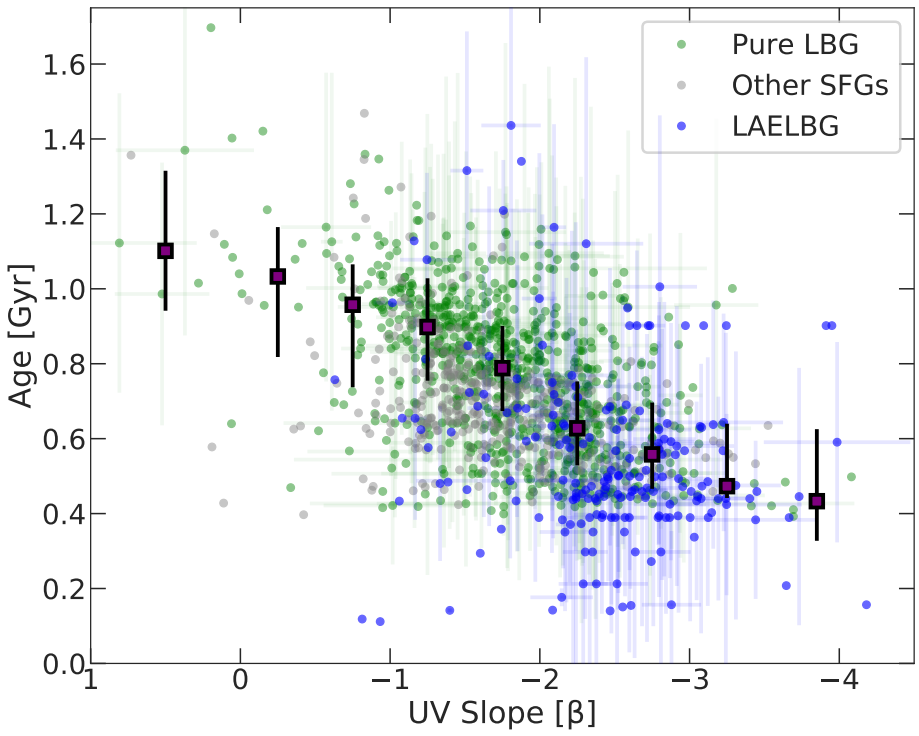

Figure 5.6: We show pure LBGs (green), LAELBGs(blue) and *Other SFGs* gray. As in Fig. 5.5 we show median values with squared markers. Overall we find a correlation with redder UV slopes coming from older galaxies.

can conclude that a dust-free ISM is key for Lyman-α to escape and be detected.

5.3 Main sequence: SFR and Stellar Mass

The main physical properties, SFR and stellar mass ($M_{\odot}$), that can be derived from the UV continuum and the IR, highlight clear differences between the pure LBG (and *Other SFGs*) and LAE-LBG populations. Since the pure LAE sample by definition does not have photometry measurements, we are not able to study these properties for them. One way to do this, as we mentioned before, would be by stacking the HST images as in Maseda et al. (2018), obtaining some constraint on the physical properties of pure LAEs. Again this isn't straightfoward due to the magnification, and recovering the source plane of would be needed.

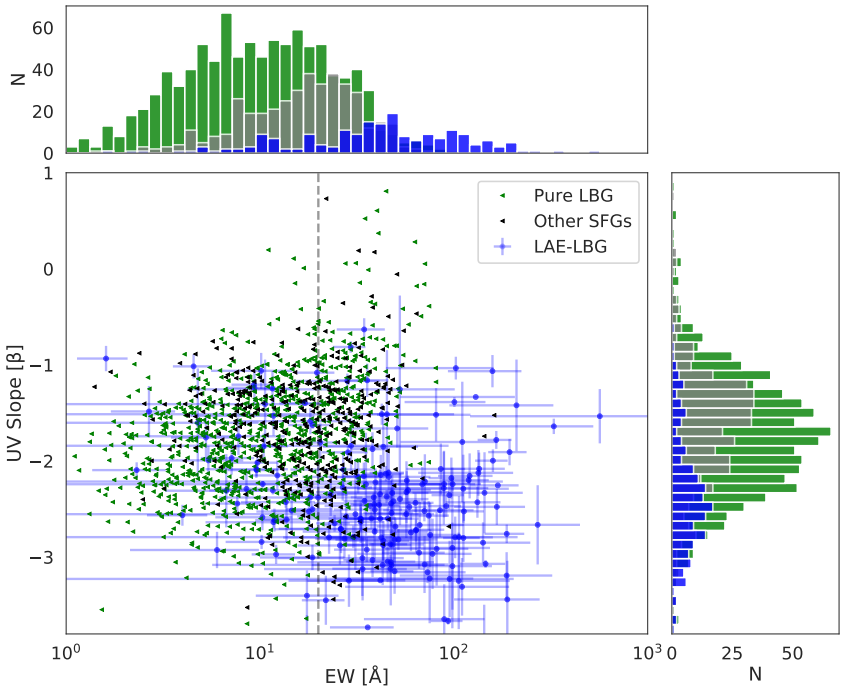

Figure 5.7: UV Slope and equivalent width for pure LBGs (green), LAE-LBGs (blue) and *Other SFGs* (gray). In the top and right are histograms for each of the axis. The locus of both populations has a clear separation, with LAE-LBGs having steeper slopes and stronger EWs.

First, in Fig. 4.5 we show the main sequence for our SFGs, comparing $\log_{10}$(SFR) to $\log_{10}$(M$\odot$). The results show that for a given stellar mass LAE-LBGs overall have a stronger SFR by $\sim$ 0.4 dex than pure LBGs; this difference is stronger at lower stellar masses and can no longer be easily seen at $\log_{10}(M_*)>8.2$. Considering that iSEDfit takes into account the parameter of wavelength dependant attenuation A(λ), we can say that overall LAEs have a stronger intrinsic star formation rate than pure LBGs (and *Other SFGs*), and this is not only due to the dustier ISM we observe (see section 5.2).

In Fig. 5.8 we show the specific star formation rate (sSFR) for the two aforementioned samples. Through all the redshift ranges, $\Delta z \sim 3$ to 7, LAEs have a stronger median sSFR than the other two regimes. We also find a larger scatter for LAEs on their sSFR values, which could be related to the many different properties needed for Lyman-α to propagate and reach the observer, as well as the LOS. The dispersion within both populations becomes much lower and the median values

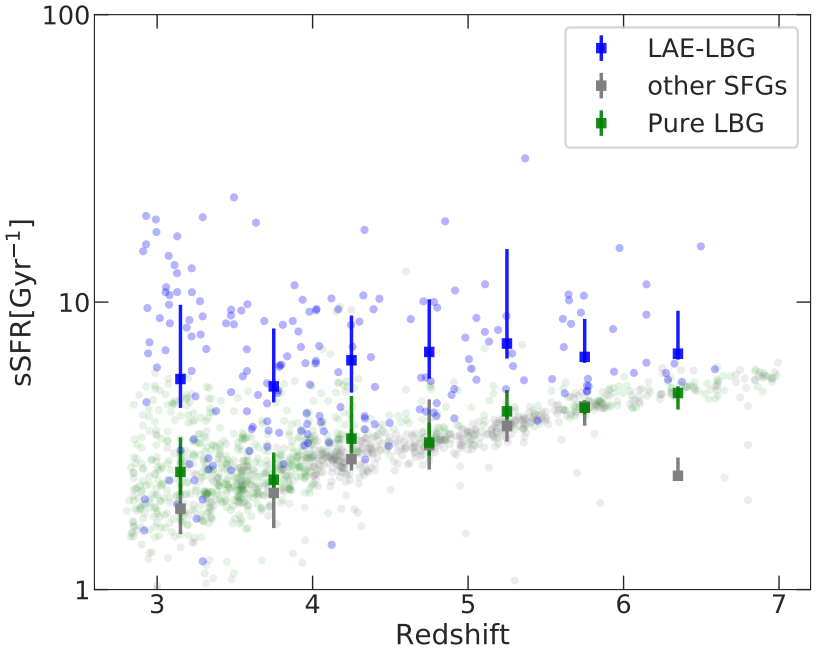

Figure 5.8: Specific star formation rate vs redshift for LAE-LBGs (blue), pure LBGs (green) and *Other SFGs* (gray). We show the median values as squares for redshift bins of $\Delta \sim 1$, with the error bars shown representing the scatter inside each bin. We see stronger median sSFR for the LAE-LBG. A higher scatter in LAE-LBGs could be related to the many different conditions needed for a Lyman-α photon to escape.

are similar at higher redshifts, which could imply that their physical properties are not as different and the LOS could be the main cause of the presence or lack of Lyman-α. This shouldn't be a surprise, since we expect high redshift galaxies to be dust-poor. Also selection bias might play a part in this result, since for high redshift sources we might not be able to detect intrinsically faint galaxies without a strong magnification due to lensing, so the sSFR of high redshift galaxies probably suffers from bias, similar to the case of Fig. 5.2, where there is an over representation of UV bright high-redshift pure LBGs and *Other SFGs*.

There is no clear difference between the sSFR of pure LBGs and *Other SFGs* in Fig. 5.8. The higher number of pure LBGs at z~3 is due to the poorly constrained color criteria selection at this redshift.

5.4 Lyman-α asymmetry and Broadness

The asymmetry and broadness results shown in Fig. 5.9 indicate some dependency between asymmetry and broadness, where broader profiles also tend to have most of their flux to the right of the line's peak (redder), correlating the shape of the profile to the velocity component of the line. Nonetheless the spread is large, and there are just a handful of galaxies which do not follow the correlation, but they are mainly due to contaminated or weak Lyman-α profiles, which produces outliers with uncharacteristic and noisy Lyman-α profiles. The main characteristic that would return a negative $\lambda_{50th} - \lambda_{peak}$ is the blue peak from a double peaked Lyman-α, we can say that galaxies with a higher HI gas velocity component due to a combination of outflows in star-forming regions, rotational velocity and inflowing material, will produce a broader Lyman-α profile, which may lack the presence of a blue peak. We believe this may happen due to higher velocities broadening the profile, shifting the emission to the wings of the line, making the blueshifted side suffer even more from extinction. We also expect a lack of double peak Lyman-α profiles at higher redshifts where the higher density of neutral hydrogen in the IGM would obscure the blue Lyman-α peak. The blue peak would only reach the observer if it is emitted from a galaxy with a very high escape fraction of ionising photons (Meyer et al. (2020)), and/or from a protocluster of fainter sources, both of which would form a ionised bubble.

Looking at the histograms in Fig. 5.9, there is a slight difference between populations, with pure LAEs overall having bluer profiles and a lower velocity component, but this difference is small, 0.17Å and $18.6 km/s$ respectively (see Table 4.1). This could be attributed to pure LAEs overall being less massive than LAE-LBG, and therefore we would expect a smaller HI column density factor which would produce a narrower profile, as well as a smaller participation of rotational velocity in the velocity component.

In Fig. 5.10 we can see that both broadness and asymmetry slightly increase with Lyman-α luminosity and M_{1500UV}, implying galaxies with a higher escape fraction of Lyman-α also tend to be affected greatly by resonant scatter from both the velocity component and column density of the HI gas. Nonetheless, it is not straightforward to separate the importance of outflow velocity and

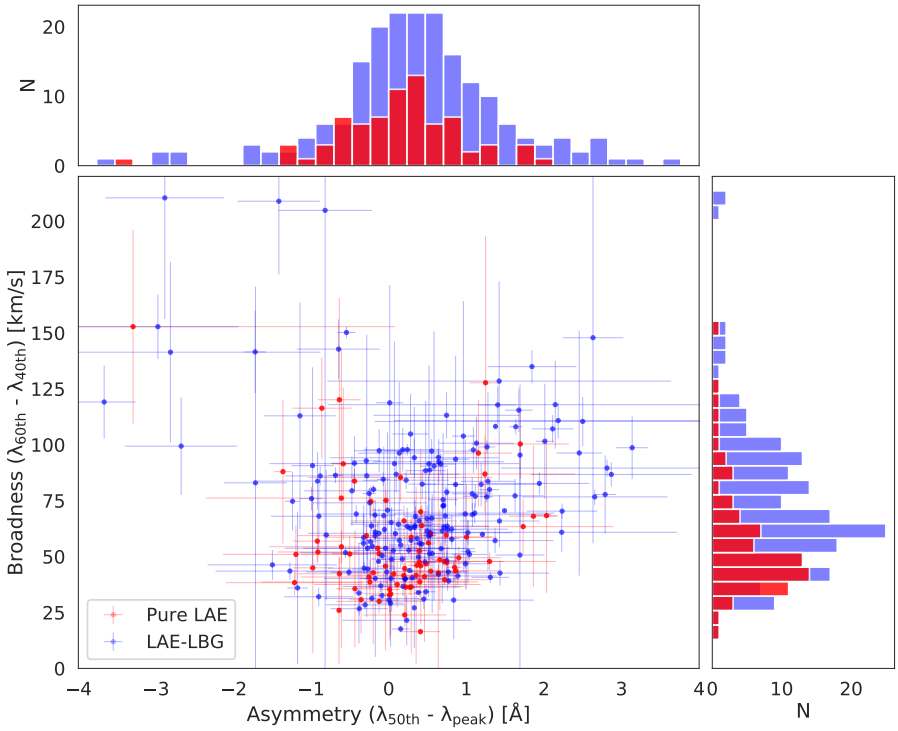

Figure 5.9: Comparison between the quantified asymmetry and broadness of the Lyman-α profile, with pure LAEs in red and LAE-LBGs in blue. On the top and the right are shown the histograms for the asymmetry and the broadness respectively. Profiles with a $\lambda_{50th} - \lambda_{peak} > 0$ have most of their flux to the right of line's peak (redder), while a value < 0 has more flux to the left of the peak (bluer). Objects with extreme values are mainly due to contaminated Lyman-α profiles, which result in highly broad and bluer asymmetric profiles.

HI column density, an in-depth study of radiative transfer simulations of Lyman-α are needed to separate the importance of both of these parameters.

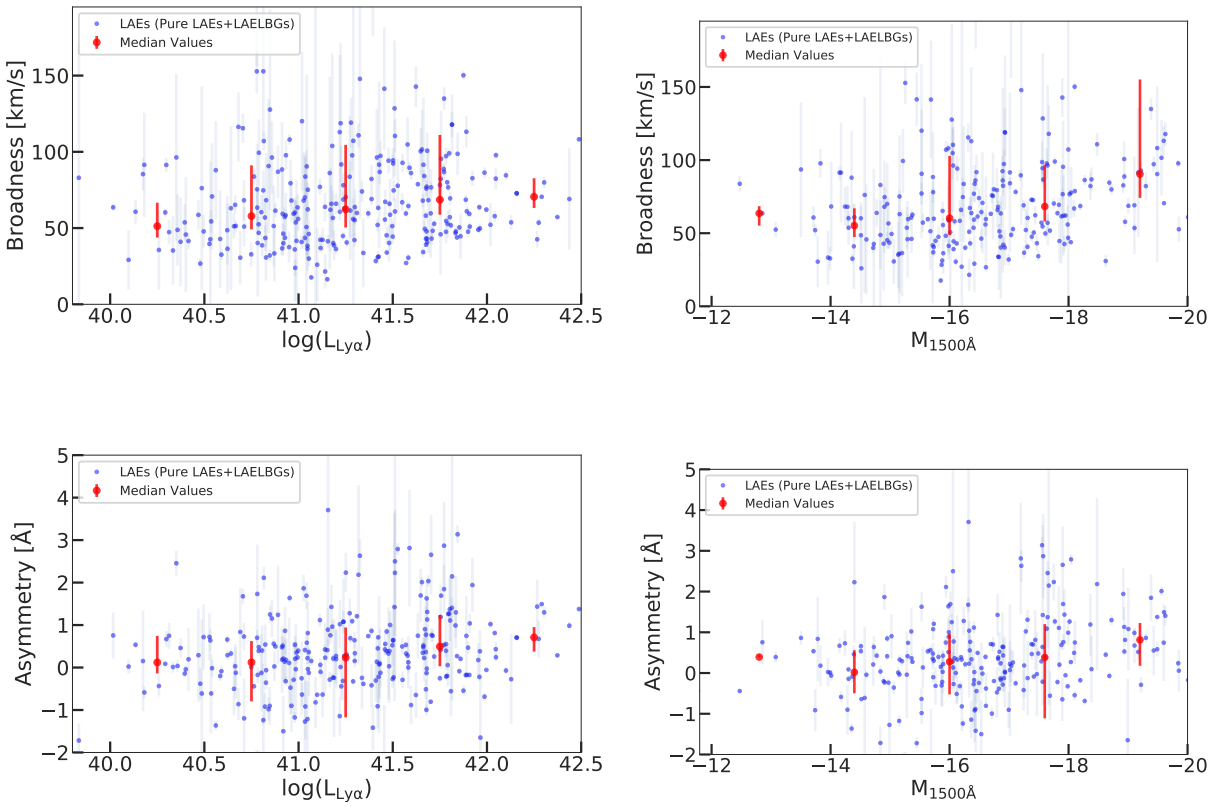

Figure 5.10: We show the reported (See Fig. A.2 and Fig. A.1) values for broadness (top) and asymmetry (bottom) against their Lyman-α emission (left) and M_{1500UV}. We show values for all LAEs (Pure LAEs and LAE-LBGs) and their median values for bins of $\Delta\log_{Ly\alpha}$ =1 and ΔM_{1500UV}=1.6 . We show 1σ error bars for each bin. A slight increase is reported for asymmetry and broadness with Lyman-α emission and M_{1500UV}, but there is a strong dispersion for both values.

Chapter 6

Conclusions and future work

In this work we have studied three regimes of SFGs: pure LBGs, pure LAEs, and LAE-LBGs, as well as *Other SFGs* which do not fall into any of these categories. We used spectra obtained from MUSE/VLT and HST photometry from Abell 370, Abell 2744 and MACS0416. We focused on understanding the differences and similarities between these galaxies, with our main focus on studying their Lyman-α profile, UV continuum and other physical properties that could be derived from their photometry such as SFR and M_*. We summarize our results as follows.

In agreement with de La Vieuville et al. (2020), we report a great diversity of high-redshift SFGs, with a spread of ~ 2 dex in Lyman-α luminosity for a given M_{1500} value. We find an absence of galaxies above the $\sim$ 1:1 SFR(Lyα)=SFR(UV) with M_{1500} <-18, implying that such massive galaxies might be obscured in Lyman-α due to dust as a byproduct of star formation, possibly falling out of the LAE regime and into the pure LBG classification. We find most pure LAEs lie near the 1:1 SFR line, with log(Lyα)<42.0, implying that it is unlikely to have stronger Lyman-α emissions without a bright UV continuum that photoionizes the hydrogren.

Our strongest finding is the difference between the UV slope distribution of LAE-LBGs and pure LBGs. We report a median value of β=-2.44 and β=-1.75 respectively. From this result we conclude that overall pure LBGs have a dustier ISM that prevents the propagation of Lyman-α. We corroborated this result by studying the A_v extinction of our sources, drawing us to the same conclusion. Nonetheless, the age of the galaxy is also involved in the shape of the UV continuum, and we are not

able to separate both variables. We expect the line of sight to the galaxy to also play an important role in this result, but with the current approach it is not possible to determine it's participation in this multi-variable problem. From this we can successfully answer one of the remaining questions of de La Vieuville et al. (2020), establishing a strong difference between pure LBGs and LAEs.

We studied the Lyman-α profile for both LAE populations via a non-parametric approach. We report a small difference between their asymmetry and broadness, 0.17 Å and 18.6 km/s respectively, with pure LAEs having overall lower velocities and a stronger bluer fraction in their profiles. We argue that this small difference may come from LAE-LBGs being more massive than pure LAEs with a stronger effect of the HI gas in the propagation of Lyman-α. Further radiative transfer simulations of Lyman-α are needed to disentangle the importance and differences of HI velocity and HI column density between pure LAEs and LAE-LBGs.

We compared the relation between SFR and stellar mass for pure LBGs and LAE-LBGs. Overall, we find double the specific star formation rate for LAE-LBGs. We also report that the higher sSFR on LAE-LBGs is present at all the studied redshifts, but the difference does decrease at earlier epochs, mostly due to a selection bias. LAE-LBGs show a strong scatter in their sSFR values, which remains at all epochs, from this we conclude that the presence of Lyman-α emission is not limited to a single cosmic epoch, there are many variables that are linked to the escape of Lyman-α.

We only find a remarkable difference between pure LBGs and *Other SFGs* for the case of the UV slope. Pure LBGs overall show bluer slopes, which might be explained due to the color criteria selection favouring galaxies with bluer and more strong UV continua.

We compared UV slope, asymmetry and broadness to Lyman-α luminosity. For each of them, we found a slight correlation to different extents. Galaxies with bluer slopes also show a stronger Lyman-α luminosity, nonetheless this trend is more strongly related to the change from pure LBG to LAE-LBG than to the strength of Lyman-α itself, with the β value being nearly independent of the luminosity of a given LAE-LBG.

For the properties of the Lyman-α profile the correlation with luminosity is stronger, we can see a difference of 0.59 Å and 19.26 km/s for asymmetry and broadness respectively. From this we can naively assume that the impact of resonant scattering and the velocity component of the HI gas is somewhat correlated with the position of a galaxy in the Lyman-α - UV plane. Galaxies with strong Lyman-α emissions will then have broader and more asymmetric profiles due to a stronger resonant scattering, which likely comes from the higher HI column densities and HI velocities. Nonetheless, these differences are small, and near the detection limits of MUSE.

Some remaining questions are left open. In specific, how the main factors of resonant scattering, HI velocity, column density, and dust attenuation vary between the two selected LAE populations. Or how these two change as Lyman-α and/or M_{1500} increases. Further work with Lyman-α radiative transfer simulations will be needed for this purpose.

Bibliography

Benitez N., 2000, The Astrophysical Journal, 536, 571–583

Bertin E., Arnouts S., 1996, A&AS, 117, 393

Bouwens R. J., et al., 2015, The Astrophysical Journal, 803, 34

Bradač M., et al., 2009, The Astrophysical Journal, 706, 1201–1212

Bradač M., et al., 2019, Monthly Notices of the Royal Astronomical Society, 489, 99–107

Calzetti D., 2001, Publications of the Astronomical Society of the Pacific, 113, 1449–1485

Castellano M., et al., 2016, Astronomy & Astrophysics, 590, A31

Chabrier G., 2003, PASP, 115, 763

Charlot S., Fall S. M., 2000, The Astrophysical Journal, 539, 718–731

Conroy C., Gunn J. E., 2010, FSPS: Flexible Stellar Population Synthesis (ascl:1010.043)

Dijkstra M., 2014, Publications of the Astronomical Society of Australia, 31

Drake A. B., et al., 2017, Astronomy & Astrophysics, 608, A6

Fontana A., D'Odorico S., Poli F., Giallongo E., Arnouts S., Cristiani S., Moorwood A., Saracco P., 2000, AJ, 120, 2206

Garavito-Camargo J. N., Forero-Romero J. E., Dijkstra M., 2014, The Astrophysical Journal, 795, 120

Gronke M., Bull P., Dijkstra M., 2015, The Astrophysical Journal, 812, 123

Gurung-López S., Orsi A., Bonoli S., 2019, Monthly Notices of the Royal Astronomical Society, 490, 733–740

Hashimoto T., et al., 2017, Astronomy & Astrophysics, 608, A10

Hinton S., Davis T. M., Lidman C., Glazebrook K., Lewis G., 2016, Astronomy and Computing, 15, 61–71

Hu W., et al., 2021, Nature Astronomy, 5, 485–490

Ishigaki M., Kawamata R., Ouchi M., Oguri M., Shimasaku K., Ono Y., 2018, The Astrophysical Journal, 854, 73

J. Bouwens R., et al., 2016, The Astrophysical Journal, 833, 72

Jauzac M., et al., 2014, Monthly Notices of the Royal Astronomical Society, 443, 1549–1554

Jauzac M., et al., 2015, Monthly Notices of the Royal Astronomical Society, 452, 1437–1446

Kawamata R., Ishigaki M., Shimasaku K., Oguri M., Ouchi M., 2015, The Astrophysical Journal, 804, 103

Khochfar S., Silk J., 2010, Monthly Notices of the Royal Astronomical Society: Letters, 410, L42–L46

Koekemoer A. M., et al., 2014, in American Astronomical Society Meeting Abstracts #223. p. 254.02

Leclercq F., et al., 2017, Astronomy & Astrophysics, 608, A8

Livermore R. C., Finkelstein S. L., Lotz J. M., 2017, The Astrophysical Journal, 835, 113

Lotz J., et al., 2014, in American Astronomical Society Meeting Abstracts #223. p. 254.01

Lotz J. M., et al., 2017, The Astrophysical Journal, 837, 97

Madau P., 1995, ApJ, 441, 18

Maiolino R., et al., 2008, Astronomy & Astrophysics, 488, 463–479

Maseda M. V., et al., 2018, The Astrophysical Journal, 865, L1

Mason C. A., Gronke M., 2020, Monthly Notices of the Royal Astronomical Society, 499, 1395–1405

Matthee J., Sobral D., Gronke M., Paulino-Afonso A., Stefanon M., Röttgering H., 2018, Astronomy & Astrophysics, 619, A136

McLure R. J., et al., 2013, Monthly Notices of the Royal Astronomical Society, 432, 2696–2716

Merlin E., et al., 2016, Astronomy & Astrophysics, 590, A30

Meurer G. R., Heckman T. M., Calzetti D., 1999, The Astrophysical Journal, 521, 64–80

Meyer R. A., Laporte N., Ellis R. S., Verhamme A., Garel T., 2020, Monthly Notices of the Royal Astronomical Society, 500, 558–564

Moustakas J., 2017, iSEDfit: Bayesian spectral energy distribution modeling of galaxies, Astrophysics Source Code Library (ascl:1708.029)

Oguri M., 2010, Publications of the Astronomical Society of Japan, 62, 1017–1024

Piqueras L., Conseil S., Shepherd M., Bacon R., Leclercq F., Richard J., 2017, MPDAF - A Python package for the analysis of VLT/MUSE data (arXiv:1710.03554)

Rauch M., 1998, ARA&A, 36, 267

Richard J., et al., 2010, Monthly Notices of the Royal Astronomical Society

Richard J., et al., 2021, An Atlas of MUSE Observations towards Twelve Massive Lensing Clusters (arXiv:2009.09784)

Sánchez-Blázquez P., et al., 2006, MNRAS, 371, 703

Santini P., et al., 2017,] 10.3847/1538-4357/aa8874

Shapley A. E., Steidel C. C., Pettini M., Adelberger K. L., 2003, The Astrophysical Journal, 588, 65–89

Speagle J. S., Steinhardt C. L., Capak P. L., Silverman J. D., 2014, ApJS, 214, 15

Verhamme A., Schaerer D., Maselli A., 2006, Astronomy & Astrophysics, 460, 397–413

Verhamme A., et al., 2018, Monthly Notices of the Royal Astronomical Society: Letters, 478, L60–L65

Weilbacher P. M., et al., 2020, A&A, 641, A28

Wisotzki L., et al., 2018, Nature, 562, 229–232

de La Vieuville G., et al., 2019, Astronomy & Astrophysics, 628, A3

de La Vieuville G., et al., 2020, Astronomy & Astrophysics, 644, A39

Appendices

Appendix A

Figures

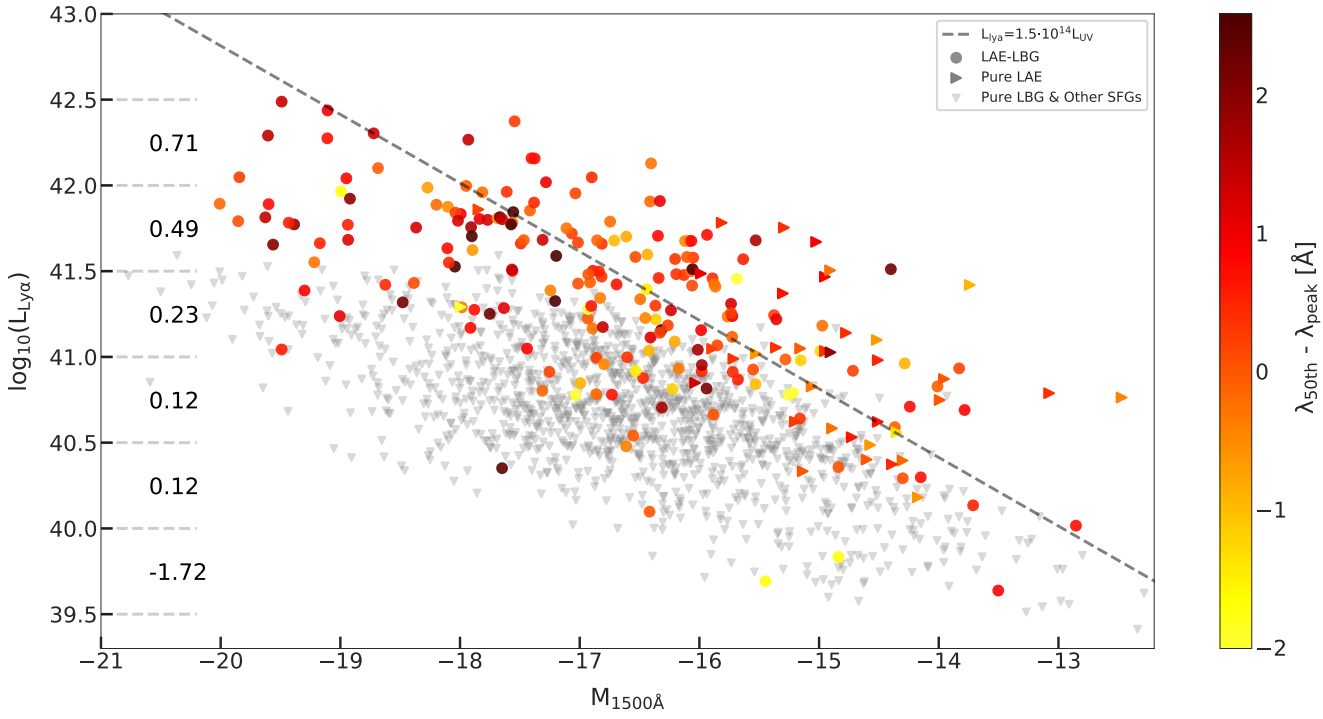

Figure A.1: As in previous figures (see Fig. 5.1 or Fig. 5.4), we use the colorbar to show asymmetry values. Pure LBGs have no Lyman-α profile measurement, we plot them in a gray color. To the right of the Y-axis we show asymetry median values [Å] grouped in Δ=0.5 bins of $\log_{10}(L_{Ly\alpha})$.

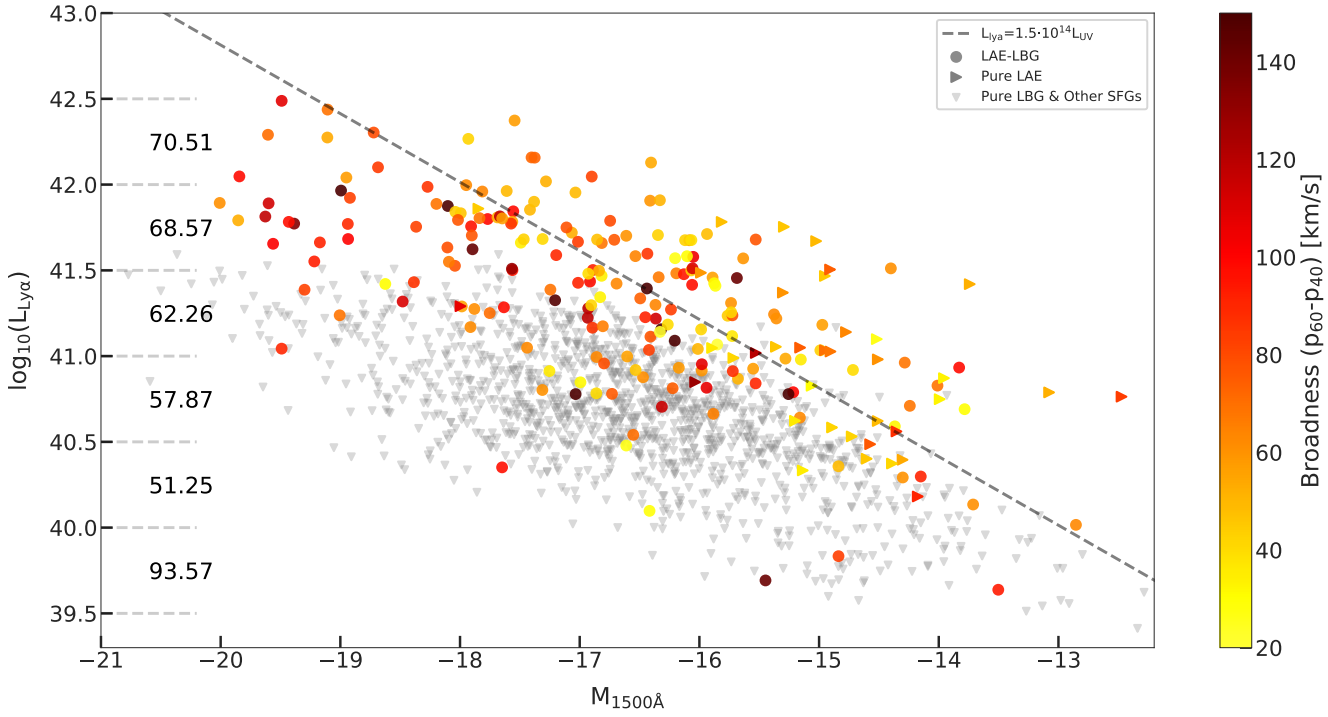

Figure A.2: As in previous figures (see Fig. 5.1 or Fig. 5.4), we use the colorbar to show broadness values. Pure LBGs have no Lyman-α profile measurement, we plot them in a gray color. To the right of the Y-axis we show broadness median values [km/s] grouped in Δ=0.5 bins of $\log_{10}(L_{Ly\alpha})$.